

Key Points:

- A wave-current coupled particle model combined with surface drifter observations were applied to reveal nearshore particle dynamics
- Winds dominate nearshore particle dynamics while effects of heat flux and waves are important as well
- Including physical effects and diminishing uncertainties are important to the improved model performance

Correspondence to:

M. Xia,
mxia@umes.edu

Citation:

Mao, M., & Xia, M. (2020). Particle dynamics in the nearshore of Lake Michigan revealed by an observation-modeling system. *Journal of Geophysical Research: Oceans*, 125, e2019JC015765. <https://doi.org/10.1029/2019JC015765>

Received 12 OCT 2019

Accepted 21 JUL 2020

Accepted article online 28 JUL 2020

Particle Dynamics in the Nearshore of Lake Michigan Revealed by an Observation-Modeling System

Miaohua Mao¹  and Meng Xia² 

¹CAS Key Laboratory of Coastal Environmental Processes and Ecological Remediation, Yantai Institute of Coastal Zone Research, Chinese Academy of Sciences, Yantai, China, ²Department of Natural Sciences, University of Maryland Eastern Shore, Princess Anne, MD, USA

Abstract Given that few drifter experiments combined with a wave-current coupled model system had been conducted in the complex nearshore area, this work was motivated to reveal the nearshore dynamics by applying an observation-modeling system to Lake Michigan. Analysis of 11 surface drifters, wind, and current observations along the lake's eastern coast indicates that their trajectories are synergistically controlled by winds and initial releasing sites. Additionally, strong winds significantly impact nearshore dynamics, and the highly sensitive nearshore and offshore drifters are stranded in distinct regions. Simulations indicate that the model reproduces drifter trajectories and endpoints reasonably and that particle fates are mainly dominated by winds, while effects from heat flux and waves are also important. Further analysis of wave effects on particle dynamics indicates that both the wave-induced sea surface roughness and Stokes drift advection are crucial to the simulated particle trajectories during wind events. Finally, virtual experiments confirm that particle dynamics are evidently susceptible to winds and initial locations. Overall, both the inclusion of physics effects (e.g., adding winds, heat fluxes, and waves) and diminishing the model uncertainties (e.g., from various wind data sources, wind drag coefficient formulations, model grids, and vertical turbulent mixing parameterizations) are important methods to improve the particle simulations. The successful application of this nearshore observation-modeling system to Lake Michigan can be beneficial to the understanding of nearshore-offshore transports and larval and fisheries recruitment success in similar freshwater and estuarine environments.

Plain Language Summary We combine surface drifter observations and computer simulations to understand movements of particles in the nearshore of Lake Michigan. Analysis of drifters' moving paths, wind, and current measurements in the summers of 2014 and 2015 indicates that drifter movements are strongly related to winds and initial releasing sites. Multiple computer programs were run to simulate the designed scenarios by artificially removing one of the influencing factors at each simulation from the model. We find that particle movements are collectively affected by winds, heat flux transfer between the air and lake water, and surface gravity waves. Further investigations demonstrate that both wave-induced sea surface roughness and Stokes drift advection are important to the simulated particle trajectories during wind events. After doing "what-if" scenarios in the computer model, distinct particle routes driven by wind-induced surface flows were simulated for virtual particles hypothetically released at various locations near the lake's southeastern coast. For example, nearshore group primarily shows longshore movements, while offshore one drifts into the deep basin. Overall, both the inclusion of physics effects (e.g., adding winds, heat fluxes, and waves) and diminishing the model uncertainties (e.g., from various wind data sources, wind drag coefficient formulations, model grids, and vertical turbulent mixing parameterizations) are important methods to improve the particle simulations. The outcome from this study will enhance the understanding of larval transport from nearshore to offshore areas in Lake Michigan and similar freshwater and estuarine environments.

1. Introduction

It is widely known that wind contributes significantly to the mean momentum dynamics and coastal circulation (Mao & Xia, 2017, 2018). Given the complexity of nearshore dynamics, a series of modeling works have been done to provide a solid foundation for understanding the synergistic effects of winds, heat flux, and river inputs on the nearshore circulation or particle dynamics (Beardsley et al., 1985; Beletsky et al., 2006; Weisberg & He, 2003; Whitney & Garvine, 2006; Xia et al., 2007) and indicated that winds influence coastal

circulation substantially that further leads to the coastal plume formations (Hickey et al., 1998; Jordi et al., 2011; Xia et al., 2010, 2011). Garvine (1985) developed a simple model and suggested that remote winds indirectly influence the adjacent shelf circulation by producing the coastal water level changes and Ekman flows, while local winds are more straightforward as their stress acts on the surface layer. In addition, density-driven circulation becomes important as the lake's thermocline deepens during the summer (Beletsky et al., 1999; Niu et al., 2015). According to the Eulerian-based modeling and observational results, Beletsky and Schwab (2008) presented the climatological circulation maps of Lake Michigan. However, their description lacks specific attention to the complex dynamics in the nearshore regions (e.g., strong longshore currents and nearshore-offshore transports).

Luckily, recent emergences of particle tracking models and drifter observations (Lumpkin et al., 2017; Van Sebille et al., 2018) help significantly enhance the understanding of circulation dynamics, especially in the complex nearshore region. McCormick et al. (2008) deployed 24 surface drifters from 2003 to 2005 in Lake Champlain, and their trajectories captured the surface flows in the coastal region successfully. As a consequence of the smaller basin size (e.g., extending 193 km in length with the widest section being less than 19 km) relative to that of the Great Lakes, the observed drifting span is short (e.g., less than 8 days). Beletsky et al. (2017) simulated particle trajectories released in the nearshore of Lake Michigan and reported that offshore particles are more accurately predicted than the nearshore ones. They further suggested that incorporations of wave-driven currents and particle movements into models are worthwhile future efforts to improve the model. Under extreme wind conditions (e.g., peak wind speeds at 26–30 m/s), wave-induced processes such as Stokes drift advection have been reported to be important in the Grand Banks (Tang et al., 2007) and Gulf of Mexico (Curcic et al., 2016). To validate the particle-tracking model and explore the complex coastal dynamics, Beletsky et al. (2006) deployed four drifters near the southwestern coast of Lake Michigan. They estimated the trajectories successfully and attributed the remaining divergence of simulations from observations to the model sensitivity to initial conditions. While this pioneering study revealed various patterns of drifter and particle trajectories (e.g., appreciable longshore movements and significant nearshore-offshore transports), it seldom focused on the forcing mechanism of particle movements resulting from winds, heat flux, river inputs, and especially surface gravity waves.

Over the past two decades, previous works have demonstrated that wave-induced effects are critical to ocean circulation and coastal dynamics (Haas et al., 2003; Yu & Slinn, 2003), especially at a localized and nearshore scale (Chen et al., 2015; Ganju et al., 2011; Lentz & Fewings, 2012). Curcic et al. (2016) investigated the surface currents and particle dynamics in the Gulf of Mexico by using a coupled model and drifter observations, which concluded that Stokes drift advection accounted for up to 20% of the averaged Lagrangian velocity during Hurricane Isaac (2011). Under strong wind conditions (e.g., maximum wind speeds of 12.8–16.3 m/s at 10-m height), recent studies from Niu and Xia (2017) and Mao and Xia (2018) specified that wave-induced sea surface roughness (Donelan et al., 1993) are mainly responsible for the offshore circulation in the shallow lake and bay. Previous studies (Niu et al., 2015, 2018) further investigated contributions of winds, density gradients, river inputs, and waves on nearshore circulation and plume dynamics in the shallow lake, but little attention was paid to a large and deep lake.

Considering the similarity of nearshore dynamics (Rao & Schwab, 2007), especially the substantial role of surface gravity waves in lake dynamics (Niu & Xia, 2017), a comprehensive understanding of nearshore particle dynamics in a large and deep lake would help gain insight into nearshore dynamics. Therefore, additional drifter and particle experiments are conducted in the current study to evaluate relative contributions of various forces (e.g., winds, heat flux, river inputs, and waves) to particle dynamics in the nearshore. Given that the model accuracy and reliability are restricted by multiple aspects of physics and uncertainties (Fringer et al., 2019; Van Sebille et al., 2018), more research is needed to distinguish between the actual improvement from physics effects versus uncertainties. Therefore, potential impacts on the particle dynamics from the obtained winds, wind drag coefficient formulation, vertical structure of currents due to model grids, and parameterizations of vertical turbulent mixing coefficient are comprehensively listed and discussed herein.

In this study, the wave-current coupled particle-tracking model along with 11 GPS-tracked surface drifter observations were combined to explore the nearshore particle dynamics. Remaining sections are organized as follows. Section 2 introduces the methodology, including the model description, data sources and field

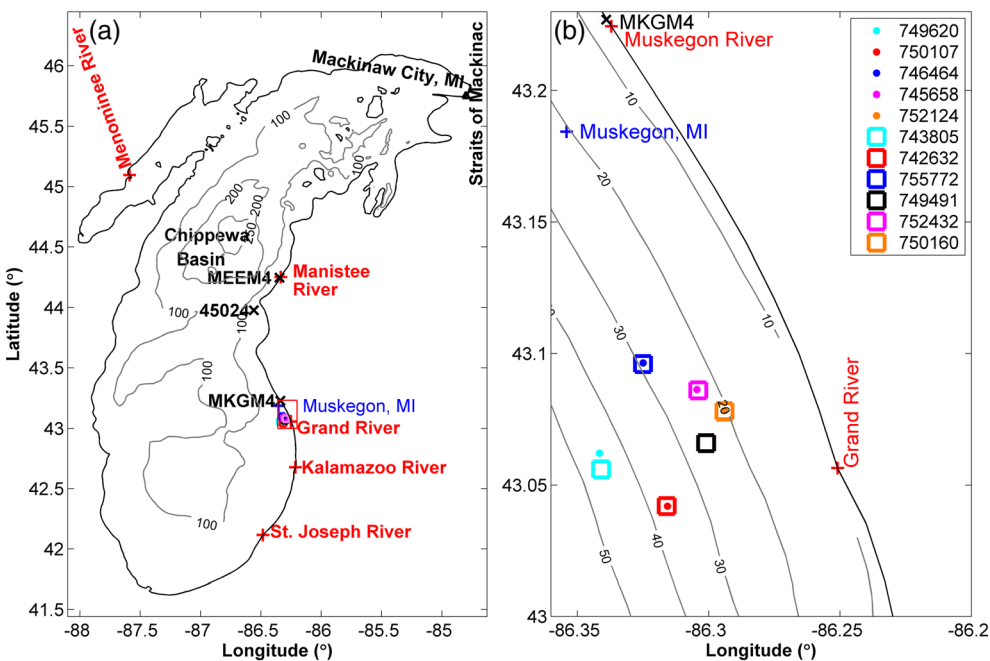


Figure 1. (a) Bathymetric contours (gray solid lines), names of main basins and straits, locations of wind buoys (black cross), ADCP (blue plus), drifters (dots and rectangles), and river inputs (red plus) of Lake Michigan; (b) shows the Grand Haven zoomed in from the red rectangle of (a) where surface drifters were deployed.

campaign, experimental design, and skill metrics. Section 3 analyzes drifter trajectories released near the lake's southeastern coast, followed by particle simulations. Section 4 discusses relative contributions of winds, heat flux, river inputs, and waves to particle dynamics, in addition to various aspects of physics effects and model uncertainties. Section 5 summarizes the results of this study and presents the conclusions.

2. Methodology

2.1. Model Domain and Grid

Lake Michigan (Figure 1) is the third largest lake by surface area ($58,000 \text{ km}^2$) and the second largest one by volume ($4,900 \text{ km}^3$) in the Great Lakes system. Its narrow and elongated body extends for a length of 494 km and a width of 190 km, with the mean and maximum water depths of 85 and 281 m, respectively. It is connected by several tributaries, including the Grand River located near the lake's southeastern coast that accounts for 13% of its entire drainage basin (Hanshue & Harrington, 2017). Given adverse effects of the offshore-directed pollutant and contaminant sources (e.g., bacteria) on the water quality and human health, coastal dynamics of the Grand River plume near its mouth have received increased attention from the Great Lakes scientists (Nekouee et al., 2013, 2015). Lake Michigan exchanges water masses with Lake Huron via Straits of Mackinac in its northeastern corner. The bi-lake exchanges were specified by including hourly water surface elevations retrieved from the National Oceanic and Atmospheric Administration's (NOAA) National Ocean Service (NOS) at Mackinaw City, Michigan along the open boundary layer (<https://tidesandcurrents.noaa.gov/stationhome.html?id=9075080>). To resolve the multiscale bathymetries and dynamics accurately with an expedient computational effort, a high-resolution model with 38,324 elements and 20,108 nodes was adopted (Mao et al., 2016). The horizontal grid was refined to 210 m near the coast, and the vertical space was resolved by using 20 uniform sigma layers.

2.2. Wave-Current Coupled Particle-Tracking Model

The modeling system is realized by a one-way off-line coupling procedure. The wind-wave model Simulating Waves Nearshore (SWAN) (Zijlema, 2010) calculates wave parameters (e.g., significant wave height, peak wave period, mean wave direction, mean wavelength, bottom wave orbital velocity, and its period) and Stokes drift advection, which are passed to the Finite-Volume Community Ocean Model (FVCOM) (Chen

et al., 2013) for the following computation of wave-induced circulation. Subsequently, the calculated Eulerian current and Stokes drift advection from FVCOM are used to drive the particle-tracking model. The modeling system applies identical horizontal grids to simulate wave dynamics, lake circulation, and particle trajectories, which avoids the interpolation errors caused by the coupling processes. The governing equations of unstructured SWAN are based on the wave action spectral energy balance (SWAN Group, 2012a, 2012b), which considers local and spatial variations, depth and current-induced wave refraction and frequency shift, wind input, nonlinear wave-wave interaction, whitecapping, bottom friction, and depth-induced wave breaking. In this study, the processes of time varying currents and water level-induced refraction and frequency shift are neglected from the one-way coupling approach. Wave effects on circulation in the wave-current coupled model (Mao & Xia, 2018) include the wave-induced roller (Svendsen et al., 2002), Stokes drift advection \vec{u}_{st} (Phillips, 1977), sea surface roughness (Donelan et al., 1993), bottom stress (Madsen, 1994), and three-dimensional radiation stress (Mellor, 2015). The three-dimensional Stokes drift advection \vec{u}_{st} and Stokes-Coriolis force $f\vec{u}_{st}$ were included in the continuity and momentum balance equations of the coastal ocean model (Lentz & Fewings, 2012). The details on how the various wave-current physics terms change the momentum equation can be referred to Appendix A.

FVCOM is integrated using a mode-split solver, in which the external and internal time steps are 4 and 16 s, respectively. Vertical and horizontal mixing processes are handled by the modified MY-2.5 turbulence closure model (Galperin et al., 1988) and the eddy parameterization scheme (Smagorinsky, 1963). The horizontal diffusion and bottom roughness length scale are set at a multiplier of 0.1 and a constant length of 0.1 cm. The air-sea transfers of heat flux and momentum are specified via the lake's surface boundary layer. Hydrodynamic simulations are initialized with a spatially uniform temperature of 4°C and a salinity and current velocity of 0. Hourly Eulerian current velocity and Stokes drift advection at the computational elements from FVCOM are interpolated to the particle locations of the particle-tracking model, in which time intervals for the scheme resolution and horizontal random walk are set at 60 and 5 s, respectively. The two-dimensional (i.e., no vertical displacement) particle-tracking model solves the nonlinear differential equation $(dx^{\rightarrow})/dt = \vec{v}(\vec{x}(t), t)$, where \vec{x} and $\vec{v}(\vec{x}, t)$ are the particle location and velocity vector at time t with an explicit fourth-order Runge-Kutta multistep method (Chen et al., 2013).

2.3. Data Sources and Field Campaign

Model bathymetry was retrieved from the NOAA-National Geophysical Data Center's 6-arc sec data (<http://www.ngdc.noaa.gov/mgg/greatlakes/greatlake.html>). The wind field was derived from the NOAA Great Lakes Environmental Research Laboratory's (GLERL) observation-based hourly data, which were processed using the Natural Neighboring Method (NNM) (Jensen et al., 2012; Schwab & Morton, 1984) (data are available upon request to Gregory Lang of NOAA-GLERL). The 3-hourly, 10-km products of air temperature and pressure, relative humidity, downward shortwave and longwave radiation fluxes, and wind speed were collected from the Global Environmental Multiscale Model (GEM) (Côté et al., 1998). The hourly reanalyzed products from the National Centers for Environmental Prediction's Climate Forecast System Version 2 at ~23-km resolution, which assimilate observations from the surface, upper balloons, aircrafts, and satellites, were used to examine the uncertainties in the obtained winds (Saha et al., 2014). Hourly water surface elevation at Mackinaw City, Michigan, and daily river inputs were collected from the NOS and U.S. Geological Survey (USGS). Five major river flows (i.e., Grand, St. Joseph, Menominee, Kalamazoo, and Manistee Rivers) accounted for 27%, 19%, 19%, 12%, and 12% of the total 404-m³/s discharges in the summer of 2014. The hourly wind data at the Coastal Station MKGM4 are managed by the NOAA's National Data Buoy Center (NDBC). Acoustic Doppler current profiler (ADCP) surface current data at 30-min interval at Muskegon, Michigan (<http://www.glerl.noaa.gov/res/recon/data/2014/mich-mkg>), are maintained by Steven Ruberg of the Realtime Coastal Observation Network (ReCON). For further details on the observational data see Figure 1 and Table 1.

Five drifters in 2014 and six in 2015 were deployed in the shallow region (20- to 45-m water depths) near the lake's southeastern coast on 8 July 2014 and 30 June 2015 (Figure 1 and Table 1). Figures 2a–2c show that surface drifters are prepared, deployed, and worked in the nearshore of Lake Michigan, respectively. The surface drifter has a similar design to those used off the Northern California coast during the Coastal Dynamics Experiments (CODE) (Davis, 1985a, 1985b) and in the Gulf of Mexico during the Grand

Table 1

Locations, Depths, and Data Availability for the Observed Wind Speed, Surface Current Velocity, and Drifters in Lake Michigan

Variable	Station/drifter #	Source	Availability	Lon. (°)	Lat. (°)	Depth(m)
Wind speed in 2014	MKGM4	GLERL	Jul. 1 to Sep. 30	-86.339	43.227	7.0
	45024	UM CILER	Jul. 1 to Sep. 30	-86.559	43.977	30.3
	MEEM4	NWS	Jul. 1 to Sep. 30	-86.346	44.248	8.6
Surface current velocity in 2014	Muskegon, Michigan	ReCON	Jul. 18 to Sep. 12	-86.356	43.180	22.5
Drifter trajectory in 2014	750107	NOAA- Northeast Fisheries Science Center	Jul. 8 to Sep. 14	-86.316	43.042	36
	749620		8 Jul. to 29 Sep.	-86.342	43.062	44
	746464		Jul. 8 to Sep. 30	-86.325	43.096	29
	745658		Jul. 8–31	-86.304	43.086	22
	752124		Jul. 8–16	-86.294	43.078	20
Drifter trajectory in 2015	743805	NOAA- Northeast Fisheries Science Center	Jun. 30 to Jul. 31	-86.341	43.056	45.1
	742632		Jun. 30 to Jul. 7	-86.316	43.042	36.6
	755772		Jun. 30 to Jul. 31	-86.325	43.096	29.6
	749491		Jun. 30 to Jul. 3	-86.301	43.066	24.4
	752432		Jun. 30 to Jul. 22	-86.304	43.086	22.3
	750160		Jun. 30 to Jul. 2	-86.294	43.078	19.5

Lagrangian Deployment experiment (GLAD) (Coelho et al., 2015; Curcic et al., 2016). Each drifter comprises a bullet buoy and GPS transmitter exposed to the air, in addition to four cross-shaped vanes at 1 × 1-m size supported by the aluminum frame and submerged in the water (Figure 2a). Both the spatial resolution and precision of the GPS-tracked drifters are about 10 m. Drifter locations are recorded hourly/every 2 hr in the summer of 2014/2015. These data are maintained online (<http://www.nefsc.noaa.gov/drifter>) by J. Manning of the NOAA's Northeast Fisheries Science Center. This kind of drifter has been successfully applied to Lake Huron (Nguyen et al., 2014), but the time span of drifter observations conducted in Lake Huron is significantly less than that of the current study in Lake Michigan (e.g., <3 days vs. up to 3 months). Based on water depths of the releasing sites, drifters are classified into offshore groups (749620, 750107, 74646, 743805, 742632, and 755772 at 29–45 m) and nearshore ones (745658, 752124, 749491, 752432, and 750160 at 20–24 m).

2.4. Design of Numerical Experiments

The default high-resolution model (Case A1 in Table 2) was driven by the spatially varying NNM winds with the inclusion of heat flux, river inputs, and waves. The wind effects were investigated by excluding all, local, and remote winds, respectively (Cases B1–B3). For convenience, the remote and local winds are defined as the spatial wind fields outside and within the Grand Haven regions (i.e., longitude of 86.36–86.2°W and latitude of 43–43.23°N) where surface drifters were released (Figure 1). Figure 3 depicts winds on the starting day of drifter movements in the summers of 2014 and 2015, and it can be seen that their speeds vary spatially. Initial local wind conditions in the beginning day of the drifter experiment in 2014 are stronger than that in 2015 (e.g., 4 vs. 2 m/s). Simulations by switching off heat flux (Case C1) and river inputs (Case D1) were added to examine their respective effects on particle dynamics. To explore impacts of waves on particle dynamics, numerical runs without waves and with partial wave-induced effects (Cases E1–E6) were included.

In accordance with realistic drifter movements, virtual particles are fixed at 0.5-m water depth below the lake surface, and their starting time and locations are initialized to be identical as the corresponding drifters. To solve the complex and chaotic nature of particle tracks, an ensemble of simulated particles was released within a region around the actual float deployment. Specifically, the initial location of each drifter was represented by 121 simulated particles (i.e., 11 × 11 gridded points with 1-m spatial interval) around the actual

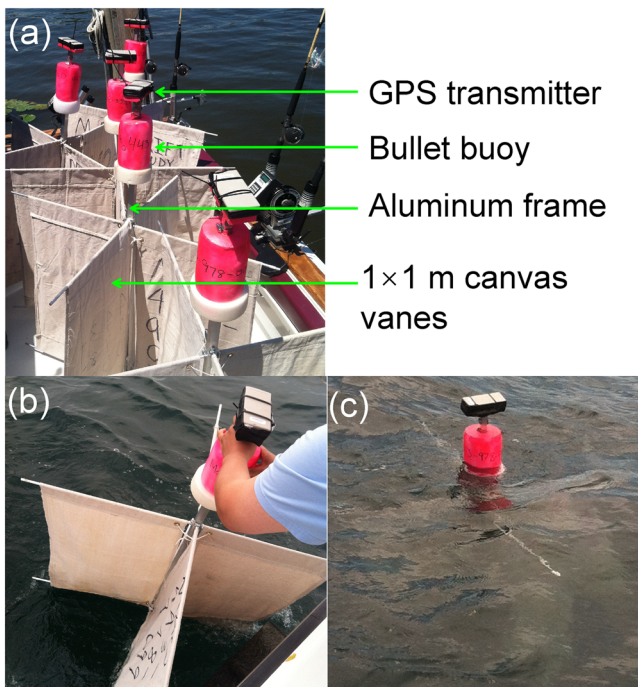


Figure 2. Surface drifters are (a) prepared, (b) deployed, and (c) worked in the nearshore of Lake Michigan; drifter structures are also indicated in (a).

Table 2
Designed Numerical Experiments in the Summer of 2014

Case	Winds	Heat flux	River inputs	Waves
A1	Yes	Yes	Yes	Yes
B1	No	Yes	Yes	No
B2	Remote	Yes	Yes	Yes
B3	Local	Yes	Yes	Yes
C1	Yes	No	Yes	Yes
D1	Yes	Yes	No	Yes
E1	Yes	Yes	Yes	No
E2	Yes	Yes	Yes	Wave-induced radiation stress off
E3	Yes	Yes	Yes	Wave-induced surface roughness off
E4	Yes	Yes	Yes	Wave-induced bottom stress off
E5	Yes	Yes	Yes	Wave-induced Stokes drift advection off
E6	Yes	Yes	Yes	Wave roller off

float location. Half of the particles, whose endpoints are relatively closer to each other than the rest, are selected to estimate a statistical representation of the float outcomes. In light of the uncertainties and the sensitivity to initial conditions, the statistical representation is considered to be a fair method to judge the model's skill. To further analyze particle dynamics and the nearshore-offshore transport, 1-month Lagrangian trajectories of 36 individual particles were released near the lake's southeastern coast in the summer of 2014.

2.5. Skill Metrics

Statistical scores of the Pearson correlation coefficient (CC), relative separation distance (RSD), and the normalized Fourier norm (F_n ; Schwab, 1983) were used to evaluate the model's skill:

$$CC = \frac{\frac{1}{N} \sum_{n=1}^N (Obs_n - \overline{Obs})(Model_n - \overline{Model})}{\sigma_{Obs_n} \sigma_{Model_n}}, \quad (1)$$

$$RSD = \frac{d_n}{\sum_{i=1}^n l_{oi}}, \quad (2)$$

$$F_n = \left(\frac{1}{N} \sum_{n=1}^N |\vec{v}_o - \vec{v}_m|^2 \right)^{\frac{1}{2}} / \left(\frac{1}{N} \sum_{n=1}^N |\vec{v}_o|^2 \right)^{\frac{1}{2}}, \quad (3)$$

where \overline{Model} and \overline{Obs} are the averaged values from the model ($Model_n$) and observation (Obs_n) in a sample of size N . The indices $i = 1, \dots, N$ denote the measurement at time step i along a drifter trajectory, and l_{oi} means the distance between the current and last position of the observed drifter. RSD is the separation distance of the endpoint (d_n) between particles and drifters normalized by the drifter's total traveling distance ($\sum_{i=1}^n l_{oi}$). The adoption of RSD eliminates the bias caused by various traveling distances among all drifters. \vec{v}_m and \vec{v}_o are the modeled and observed vectors of wind speeds in a sample of size N . F_n stands for the relative variance unexplained by the model, of which the reasonable range is 0–1; a smaller value indicates a better skill (e.g., 0 means a perfect estimation).

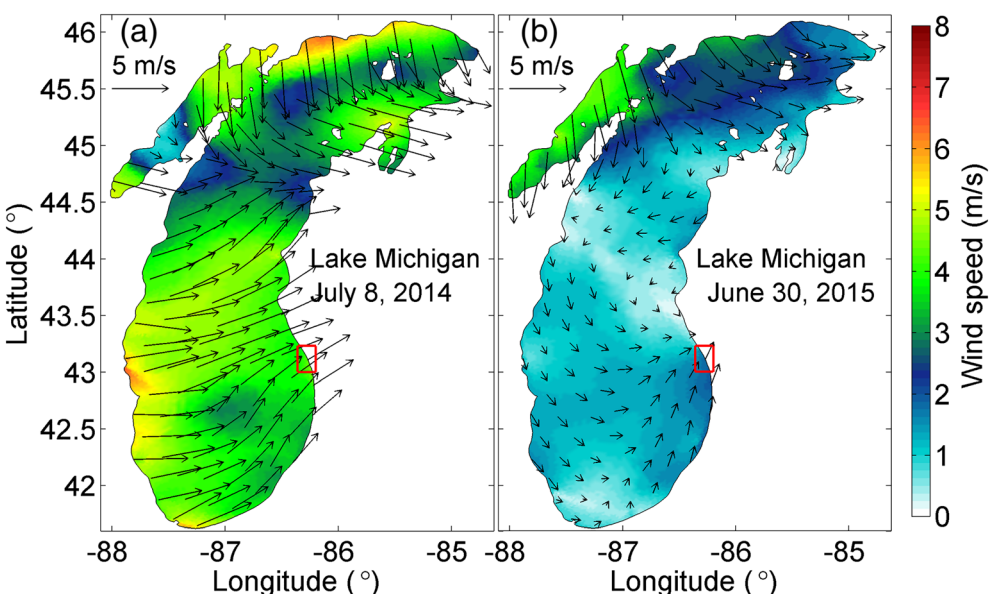


Figure 3. Spatial wind fields in Lake Michigan at the beginning day, when drifters were released on (a) 8 July 2014 and (b) 30 June 2015. The red rectangular area denotes Grand Haven.

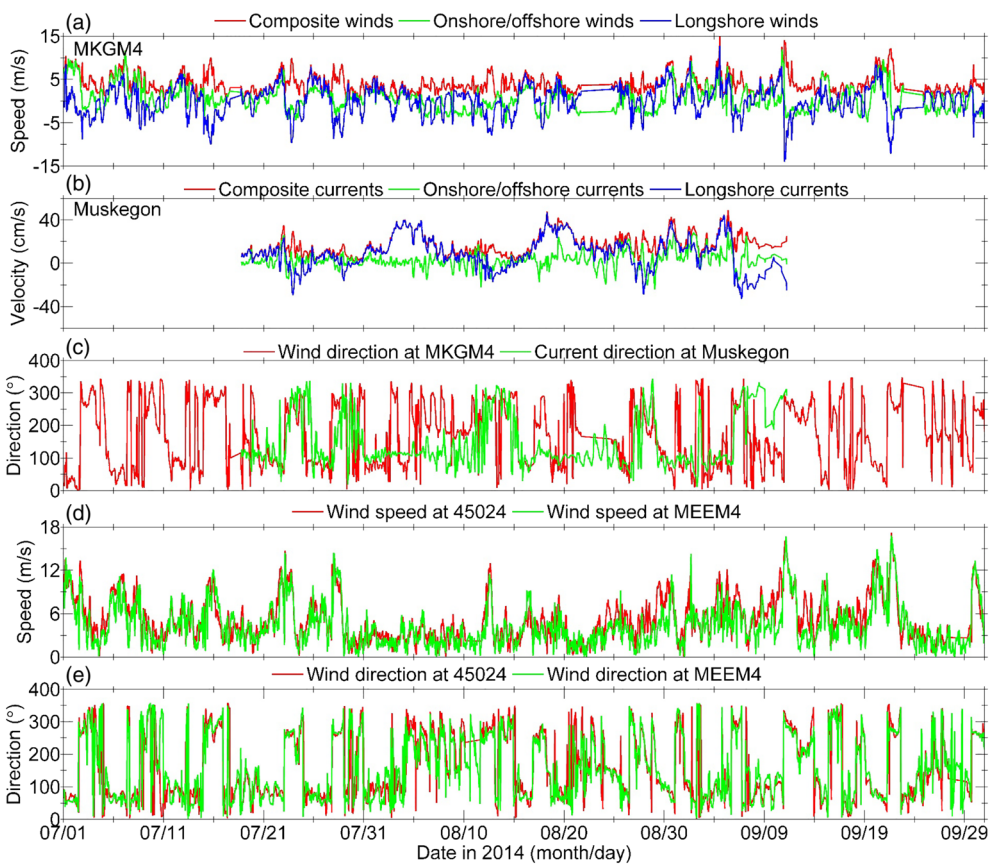


Figure 4. Time series of the observed (a) wind speed at MKGM4, (b) current velocity at Muskegon, (c) wind direction at MKGM4 and current direction at Muskegon, in addition to (d) wind speed and (e) direction at 45024 and MEEM4.

3. Drifter Observations and Numerical Experiments

3.1. The Relationship Between Wind Forcing and Current Velocity

Figure 4 shows the observational wind speed and current velocity during the summer of 2014 from the Buoy Station MKGM4 and ADCP measurements near the lake's southeastern coast. The Pearson CC between the onshore wind and onshore/longshore currents was 0.57/0.27, while it was 0.23/0.32 between the longshore wind and onshore/longshore currents. The great CC value indicated that locally onshore winds significantly affected onshore-offshore transports (e.g., linking coastal currents with basin-scale circulation in the offshore area), while longshore winds had relatively weaker effects on longshore currents (e.g., 0.57 vs. 0.32). It should be noteworthy that longshore/onshore winds posed moderate effects on the onshore/longshore currents with CC of 0.23/0.27, presumably due to Ekman transports. Under the downcoast longshore winds and offshore currents, the current relative to the wind direction is more likely to be consistent with the Ekman transport hypothesis (Figures 4a–4c). During 19–21 August, the current velocity reached 33 cm/s under locally weak wind conditions (e.g., less than 3.1 m/s), suggesting that the remote wind was likely responsible for generating the strong coastal current. Based on the observational analysis, it can be concluded that coastal currents are mainly controlled by local winds and occasionally influenced by remote winds. To further understand coastal dynamics, a set of drifters released in the nearshore of the lake's southeastern coast were analyzed below.

3.2. Analysis of GPS-Tracked Surface Drifters

Distinct endpoints of drifters (e.g., lake's northern islands vs. southeastern coast), time spans (e.g., less than 2 weeks vs. over 2 months), and distances (e.g., 1031–1271 vs. 111–352 km for offshore and nearshore groups) in 2014 are given in Figure 5. The nearshore 752124 moved mainly along the eastern coast, which was stranded ashore after 1-week's journey, while 745658 drifted onshore within 3 weeks after initial

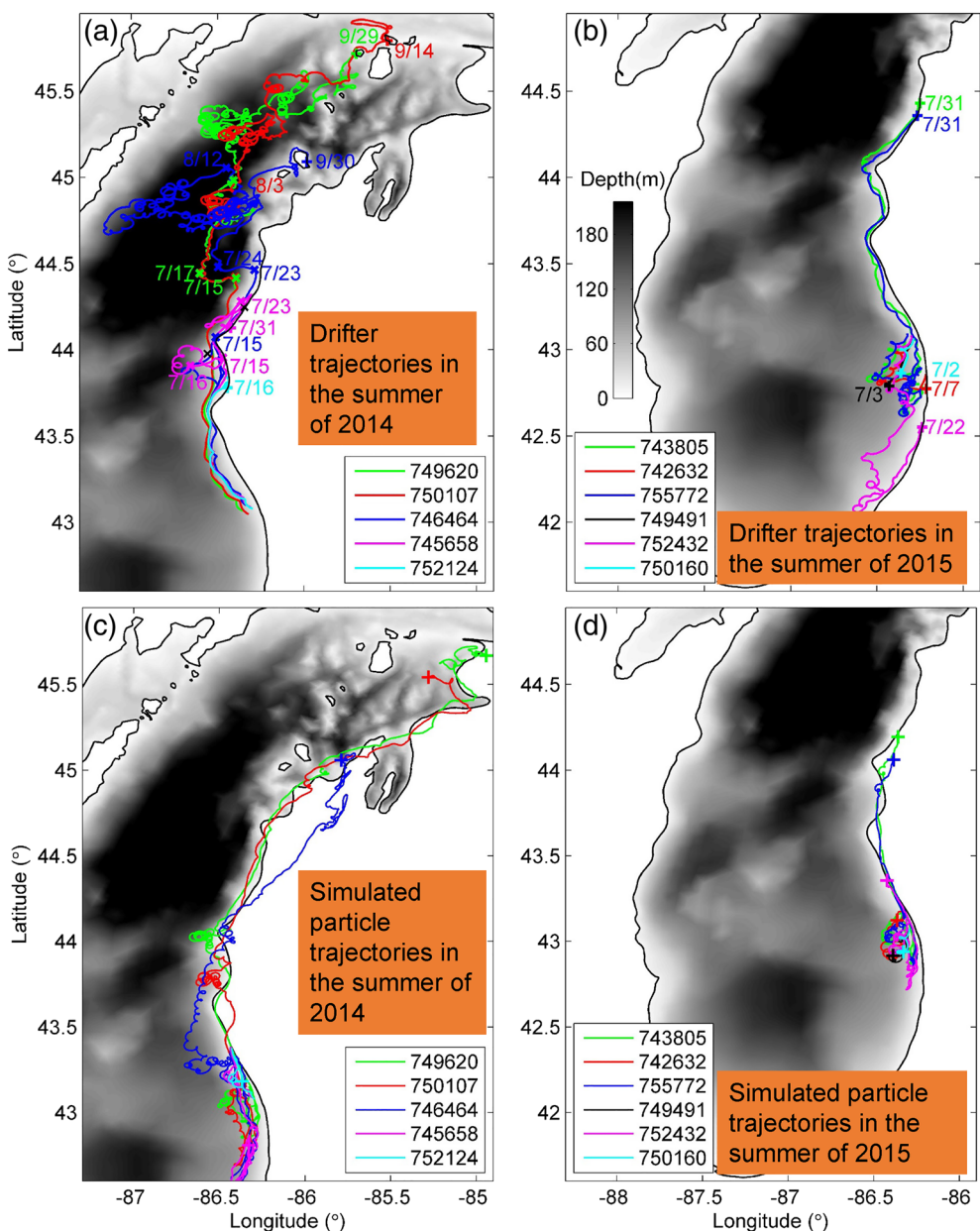


Figure 5. The GPS-tracked surface drifter trajectories in the summers of (a) 2014 and (b) 2015; the dates indicated with colored cross and plus signs show the times when discernable drifter movements are detected and stranded; (c) and (d) are simulated particles corresponding to (a) and (b), respectively.

offshore movements. Before experiencing the rotational wind switching from westerly to northerly on 23 July (Figures 4d and 4e), this nearshore drifter completed its offshore-onshore trip and longshore movement after 8 days. The initial northward drifting distance from nearshore 752124 was relatively short because of the highly dynamic and complex wind-current-bathymetry interactions in the extremely shallow regions, and its trajectory became quite complex on 14 July. Offshore 750107 and 749620 traveled 169 km at a mean speed of 32 cm/s along the coast in the first week. Steered by local winds increasing from 0.9 to 12.6 m/s during 15–17 July (Figure 4d), both drifters moved 22 km offshore at 11 cm/s and progressed northward in Chippewa Basin. The typical near-inertial motion was characterized by the trochoidal trajectories with an oscillation period (T) of 16–18 hr and a length scale (D) of ~10 km ($T = \frac{\pi}{\Omega \sin \varphi}$ and $D = \frac{V}{\Omega \sin \varphi}$, where Ω , φ , and V are the Earth rotation rate, latitude, and

current velocity, respectively) (Stewart, 2008), which is consistent with previous findings of Beletsky et al. (2006) and Troy et al. (2012). Drifter 746464 advanced around 260 km at a speed of 21 cm/s, followed by a wind-induced reversing trajectory due to the intense wind (e.g., up to 12 m/s) veering from southerly to northerly on 15 July (Figures 4d and 4e). This drifter then experienced wind-driven, offshore Ekman drift at an angle of $\sim 45^\circ$ to the right of wind direction before switching to onshore and then alongshore movements during 17–19 July. Driven by the rotational and intensified wind on 23 July (Figures 4d and 4e), this drifter abruptly moved offshore into Chippewa Basin. Drifters 750107 and 749620 departed from this basin on 3 August, while 746464 returned to the basin on 12 August.

Figure 5b depicts trajectories of six surface drifters in 2015, which shows that the Offshore Drifters 743805 and 755772 were stranded in the lake's northern shoreline, while the nearshore 752432 ran aground in the lake's southeastern coast. Drifters 749491 and 750160 stopped sending GPS signals after its 2- to 3-days' southward movement. Due to significant onshore movements after its release, the Offshore Drifter 742632 was stranded on the nearby southeastern coast. Therefore, these phenomena confirm that drifter trajectories are highly sensitive to initial locations (e.g., starting in the offshore or nearshore area). Although the initial distance between Drifters 742632 and 752432 was quite close to each other (e.g., ~ 2.2 km), distinct trajectories and endpoints driven by complex coastal currents were detected. Based on the analysis of drifter experiments, it can be concluded that the longshore movement is the initial and major drifter pattern near the coast, while near-inertial motions (e.g., spiral tracks) prevails in the offshore region. Additionally, wind forcing is mainly responsible for the occasional offshore drift. In the next subsection, performance of the particle-tracking model is validated to further investigate particle dynamics in the lake's nearshore region.

3.3. Simulated Particle Trajectories in 2014 and 2015

Figure 5c shows simulated tracks from the model in 2014, which reproduced the corresponding drifter trajectories and endpoints satisfactorily. Although the statistical description of float outcomes using an ensemble of particles shows unrealistic trajectories sometimes, it can capture the major movement patterns and endpoints of drifters well and represent the chaotic and complex nature of Lagrangian flows better. To eliminate the accumulated error along the Lagrangian trajectory, Liu and Weisberg (2011) reinitiated the particle location in accordance with the actual drifter each day and then used a separation distance to evaluate the particle-tracking model applied to the Gulf of Mexico coasts. Given that coastal drifter dynamics were highly complex without initializations, the *RSD* defined in Equation 2 was adopted. During episodic wind events, this consideration is more realistic and practical when corrections according to drifter observations are not consistently available. Because of the difficulty in reproducing the complex coastal current (Beletsky & Schwab, 2001), the ensemble-averaged *RSD* between observed and simulated particles for the offshore group was smaller than the nearshore one (e.g., 3% vs. 51%). The deviation of endpoints between simulated offshore and observed ones is mainly caused by the disparity in the offshore movement during strong wind events. On 23 July, Drifter 746464 experienced significant offshore movements with a distance of 6 km from the coast, whereas the simulated one wandered near the coast with a northward longshore movement. On 15 July, Particles 749620 and 750107 moved offshore slightly before drifting back to the coast, which failed to follow the substantial offshore movements. Huntley et al. (2011) mentioned that slight variations from the Eulerian current simulation could result in a greater displacement along the Lagrangian pathway, especially over the area where velocity gradients are steep. Given the significant influence of winds on surface currents (McCormick et al., 2002), it is critical to employ a more accurate wind field for particle simulations, such as an appropriate blending of the weather forecasted winds with the observed buoy data (He et al., 2004). Despite the highly sensitive response of particle trajectories to surface currents, the particle-tracking model still captured the near-inertial oscillations, drifter trajectories, and endpoints well.

To further validate the model's reliability, Figure 5d depicts the simulated trajectories in 2015. Results indicated that particles followed the corresponding drifter tracks reasonably, including the northward longshore movements of Offshore Drifters 743805 and 755772, as well as the movements of Nearshore Drifters 749491 and 750160. The large deviation of the endpoints between observation and simulation for 752432 was caused by the high sensitivity of particle movements to nearshore currents, resulting in large Lagrangian errors accumulated in the model (Huntley et al., 2011). Considering the difficulty in simulating coastal drifter trajectories (Beletsky et al., 2006), the performance is satisfactory with 16% and 36% *RSD* for offshore and nearshore groups. Given uncertainties in estimating the eddy diffusivity (Rypina et al., 2016), it is a rather

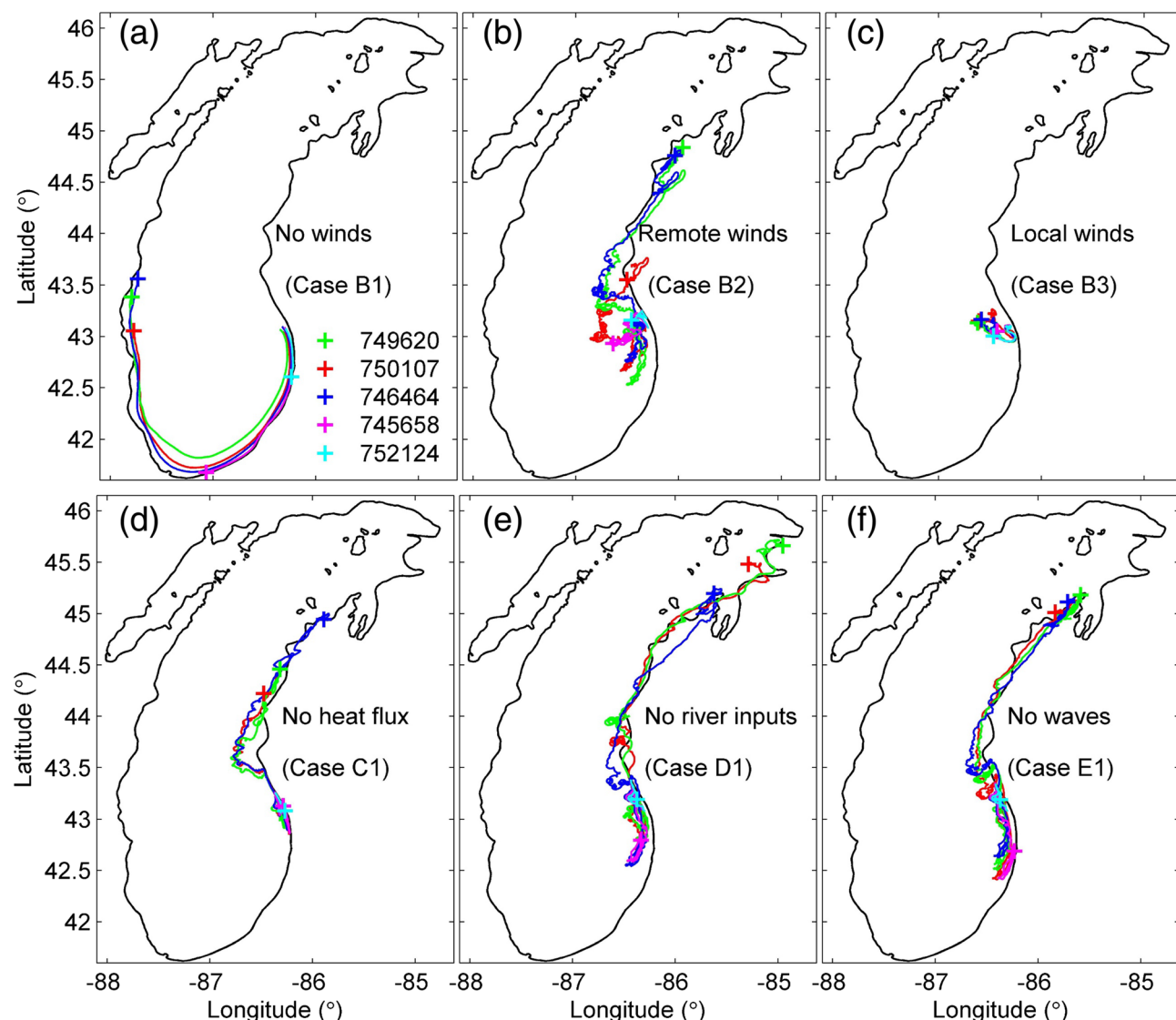


Figure 6. Simulated particle trajectories from the numerical model without (a) winds, (b) local winds, (c) remote winds, (d) heat flux, (e) river inputs, and (f) waves, respectively, in 2014.

challenging task to reproduce particle trajectories accurately. It would be worthwhile in future endeavors to deploy additional drifters for model calibration and validation (Lumpkin et al., 2017). After having examined and validated its performance, the model was applied to investigate particle dynamics with additional numerical experiments in the next section.

4. Results and Discussion

4.1. Effects of Winds, Heat Flux, and River Inputs on Particle Dynamics

Given that summer circulation patterns in Lake Michigan are mainly caused by wind and density-driven currents as the thermal stratification develops (Beletsky et al., 2006), this study first examined effects of winds and heat flux on particle dynamics. Figures 6a–6c illustrate the simulated trajectories in 2014 without all, local, and remote winds, respectively (Cases B1–B3 in Table 2). Without winds, endpoints of all offshore particles were located in the southern basin with the ensemble-averaged *RSD* increased by 33% (Table 3). Because coastal currents and subsequent particle movements are steered by winds (Beletsky et al., 2003; Xia et al., 2011), simulations using remote or local winds yielded distinct trajectories (Figure 6b) with an

Table 3

Separation Distances and Their Normalized Values (i.e., RSD) Calculated for the Drifter Experiments in 2014 During Summer and Several 2-Day Wind Events From Various Numerical Cases

Case	Model settings	RSD (%) in the summer of 2014										
		750–107	749–620	746–464	745–658	752–124	Mean					
A1	Default	3	5	1	42	60	22					
B1	No winds	34	25	17	79	119	55					
B2	No local winds	25	8	3	38	62	27					
B3	No remote winds	30	24	17	34	78	36					
C1	No heat flux	18	12	1	32	71	27					
D1	No river inputs	4	5	2	42	59	22					
E1	No waves	9	5	2	46	59	24					
Separation distance (km) in the summer of 2014												
A1	Default	30.9	62.9	12.7	147.8	66.6	64.2					
B1	No winds	350.5	314.5	216.1	278.1	132.1	258.3					
B2	No local winds	257.8	100.6	38.1	133.8	68.8	119.8					
B3	No remote winds	309.3	301.9	216.1	119.7	86.6	206.7					
C1	No heat flux	185.6	151.0	12.7	112.6	78.8	108.1					
D1	No river inputs	41.2	62.9	25.4	147.8	65.5	68.6					
E1	No waves	92.8	62.9	25.4	161.9	65.5	81.7					
RSD (%) for 749620 in 2014				Separation distance (km) for 749620 in 2014								
		July 13	July 15	July 17	July 13	July 15	July 17					
A1	Default	48	66	10	29.0	13.1	2.4					
E1	No waves	48	73	15	29.0	14.5	3.6					
E2	No wave-induced radiation stress	43	61	3	26.0	12.1	0.7					
E3	No wave-induced surface roughness	49	77	20	29.6	15.3	4.7					
E4	No wave-induced bottom stress	47	66	10	28.4	13.1	2.4					
E5	No Stokes drift advection	72	67	10	43.6	13.3	2.4					
E6	No wave-induced roller	47	66	10	28.4	13.1	2.4					
RSD (%) for the 2-day wind events in the summer of 2014												
Date drifter		July				August		September		Mean		
		13	15	17	22	9	1	4	10	19	21	
A1	749620	48	66	10	18	27	26	36	45	46	48	35
	746464	19	38	52	38	19	49	18	3	13	25	47
	Mean	29	52	31	28	20	38	22	20	29	36	32
E3	749620	49	77	20	24	20	21	18	33	44	48	37
	746464	40	54	48	38	24	43	19	6	8	28	68
	Mean	45	66	34	31	22	32	19	20	26	38	63
E5	749620	72	67	10	18	20	27	25	37	48	64	58
	746464	22	76	52	25	20	49	19	3	14	26	45
	Mean	47	72	31	32	20	38	22	20	31	45	52

increased RSD by 5% or 14%. Based on drifter trajectories in the coastal Gulf of Finland, Delpeche-Ellmann et al. (2016) concluded that the intense wind is the key factor in generating the upwelling and offshore Ekman flows that control drifter/particle movements.

Considering that particle trajectories are driven by surface currents, residual summer circulation (i.e., vector difference of current velocity) resulting from various factors is shown in Figure 7. Clearly, remote winds substantially affected the deep-lake circulation, generating the residual current up to 20 cm/s (Figure 7c). Because of substantial offshore transports for the particles from the nearshore region, deep-water circulation (e.g., gyre activity during episodic events) can indirectly influence coastal dynamics (Lee et al., 2007). It can also be seen that the nearshore circulation around the Grand Haven was influenced by both remote and local winds (Figures 7b and 7c). Remote winds affect particle dynamics in the lake's nearshore via the interaction between the lake circulation and its coastal dynamics. Although local wind-induced circulation near Grand

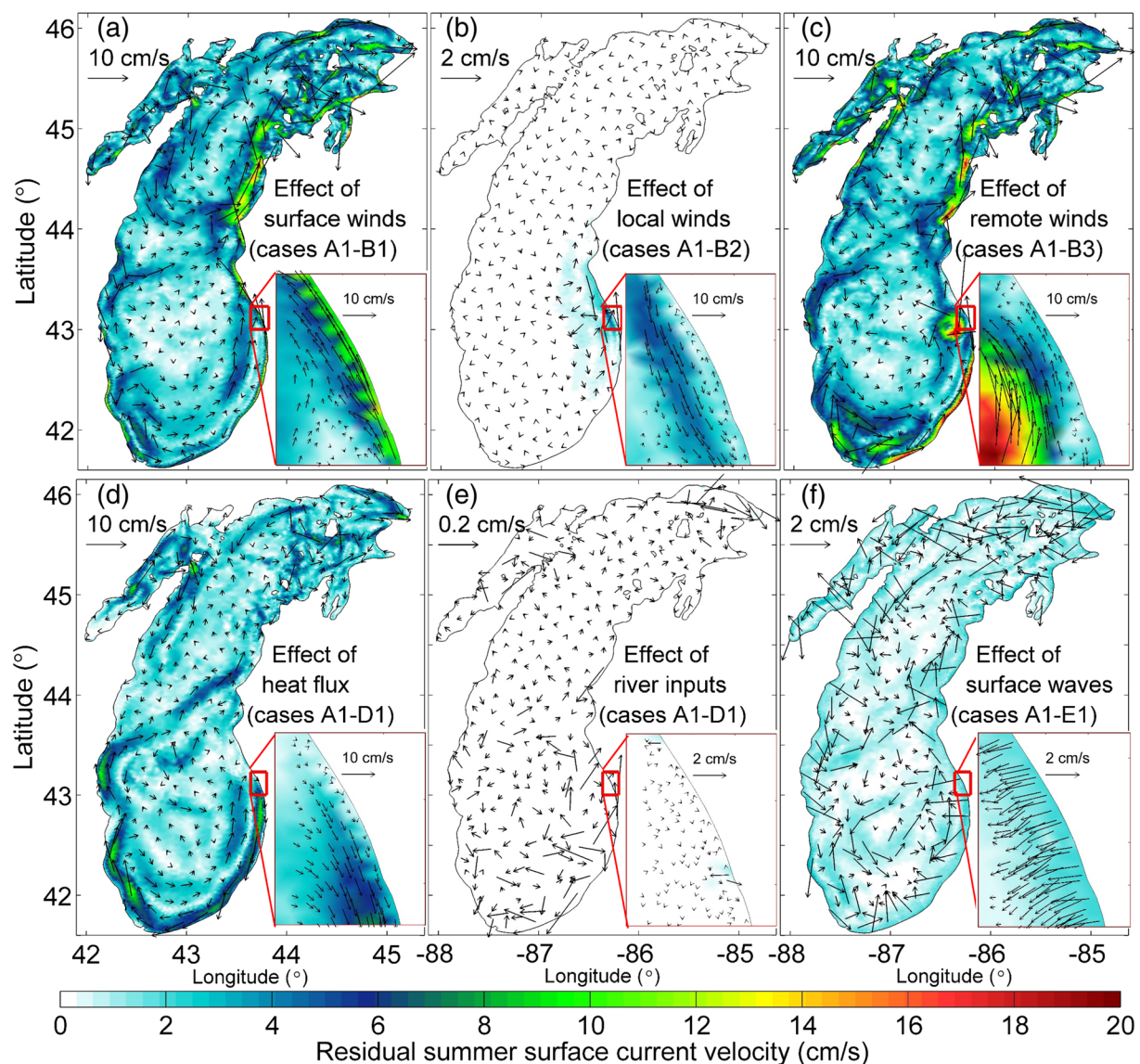


Figure 7. Simulated residual circulation (i.e., vector difference of current velocity) between the standard run (i.e., Case A1) and that without (a) winds, (b) local winds, (c) remote winds, (d) heat flux, (e) river inputs, and (f) waves in the summer of 2014.

Haven was less than 6 cm/s, it significantly influenced the particle fate released in this region (Figure 6b). These findings are consistent with previous results in coastal ocean (Xia et al., 2007, 2010, 2011), which conclude that wind forcing is a key factor to nearshore particle distributions and movements. For an accurate simulation of coastal particle trajectories, it is necessary to include both remote and local winds.

In addition to wind-driven currents, density-driven/thermal currents (Case C1) were significant to the simulated lake circulation (e.g., up to 10 cm/s in Figure 7d). However, thermal currents were relatively weak along the track of particle movements (e.g., <6 cm/s), and endpoints of offshore and nearshore groups from Case C1 were still located in the northern lake and southeastern coast, respectively. The contribution of wind-driven currents to particle movements is greater than that of thermal currents, which is consistent with the conclusion of Delpache-Ellmann et al. (2016) in their study on the coastal Gulf of Finland. Although the ensemble-averaged RSD from Case A1 to C1 increased only by 5%, the heat flux was still incorporated into the default model for accurate predictions. Without the inclusion of river inputs (Case D1), lake circulation (Figure 7e) and particle trajectories (Figure 6e) varied marginally. Prakash et al. (2007) indicated that the

Niagara River flow (6,000 m³/s) in Lake Ontario (volume at 1640 km³) significantly impacted nearby particle movements, while effects of river inputs on the particle dynamics in the current study are very limited as the river discharge into Lake Michigan is 404 m³/s. Given that a significant improvement of this work compared to the previous one (Beletsky et al., 2006) is the inclusion of wave effects, next subsection will discuss wave effects on particle dynamics in detail.

4.2. Effects of Waves on Particle Dynamics

With the inclusion of waves, the ensemble-averaged *RSD* score was improved by 2% (Table 3). During the summer of 2014, wave-induced surface currents (Figure 7f) were discernable near the coast (e.g., 2-cm/s offshore currents along the southeastern shore). To reduce the accumulated Lagrangian errors and to focus on the wave-induced effects in the highly sensitive particle-tracking model (Huntley et al., 2011), simulated particles with full, partial, and no wave effects were initialized in accordance with drifter locations before experiencing strong wind events (Figure 8). Wind events (e.g., peak wind speed at 12.1 m/s) during 13–15, 15–17, and 17–19 July were selected for preliminary analyses since typical longshore, offshore, and spiral movements of the Drifter 749620 in the shallow, intermediate, and deep-water regions were detected during these periods.

Overall, wave effects on particle trajectories were important, and contributions from wave-induced bottom stress or roller were negligible. During 13–15 July, the obliquely incident waves generated Stokes drift advection nearly in the longshore direction, which significantly affected particle movements in the nearshore. Without the inclusion of Stokes drift advection (i.e., changing from Case A1 to E5), the *RSD* increased by 24%. This finding extends the importance of Stokes drift advection from the continental shelf (Lentz & Fewings, 2012; Röhrs et al., 2012) and Gulf Coast (Curcic et al., 2016) to the lake's nearshore. Given that the breaking process is weak in the nearshore area during this particular event (e.g., wave direction is orientated along the isobaths), the wave radiation stress-induced particle movement can be ignored. However, this effect is likely significant in the nearshore under other conditions, such as waves approaching the shoreline obliquely with a strong depth-induced breaking.

By including waves (i.e., changing from Case E1 to A1), the *RSD* during 15–17 and 17–19 July were reduced from 73% and 15% to 66% and 10%, respectively (Table 3). During 15–17 July, all simulations showed quite weak offshore movements. Given that winds are primarily responsible for generating surface currents, waves, and their interaction (Mao & Xia, 2018), an accurate representation of wind fields is critical to simulating particle trajectories (McCormick et al., 2002). Future endeavor should be taken to improve the quality of offshore winds in coastal regions by incorporating more offshore wind stations into numerical models (Mayer et al., 2017). During 17–19 July, particle trajectories were mainly affected by excluding wave-induced sea surface roughness (e.g., *RSD* increased by 10% from Case E3 to A1). These results corroborate the recent finding in Lake Erie (Niu & Xia, 2017) that wave-induced sea surface roughness is important in offshore areas. In the wave-current coupled system, the wave-state dependent surface roughness (e.g., related to inverse wave age $\frac{U_{10}}{c}$, where U_{10} and c are the wind speed at a 10-m height and wave phase speed, see Equation A10 for details) has a net change of the mean wind drag coefficient C_D (Equation A9). During 17–19 July, the spatially averaged wind speed over the particle trajectory was less than 6.6 m/s, which led to a constant C_D of 1.2×10^{-3} without considering the wave effects (Equation A6). In contrast, C_D calculated based on the wave-state (e.g., inverse wave age $\frac{U_{10}}{c}$ in the range of 0.08–2.75) related surface roughness fluctuated between 0.4×10^{-3} and 1.7×10^{-3} .

To understand whether the wave-induced sea surface roughness and Stokes drift advection are indeed significant and for accurate representations in the overall model and data set results, additional numerical runs were conducted. In addition to 749620, simulated trajectories of 746464 were compared to observations, which were characterized by longshore, offshore, and spiral movements. Specifically, 2-day simulations from both drifters for 11 wind events were considered to justify the wave effects on particle dynamics (Figure 9). By including the wave-induced sea surface roughness and Stokes drift advection, improvements of the *RSD* for 746464 were up to 21% on 13 July and 21 September and 38% on 15 July, respectively (Table 3). Given that the strong northerly wind on 23 July (Figures 4d and 4e) was not well captured by the model, simulated particles showed a weaker, wind-driven offshore movement than that observed from the drifter (Figure 9dl). On average, the wind-induced sea surface roughness or Stokes drift advection improved the ensemble-averaged *RSD*

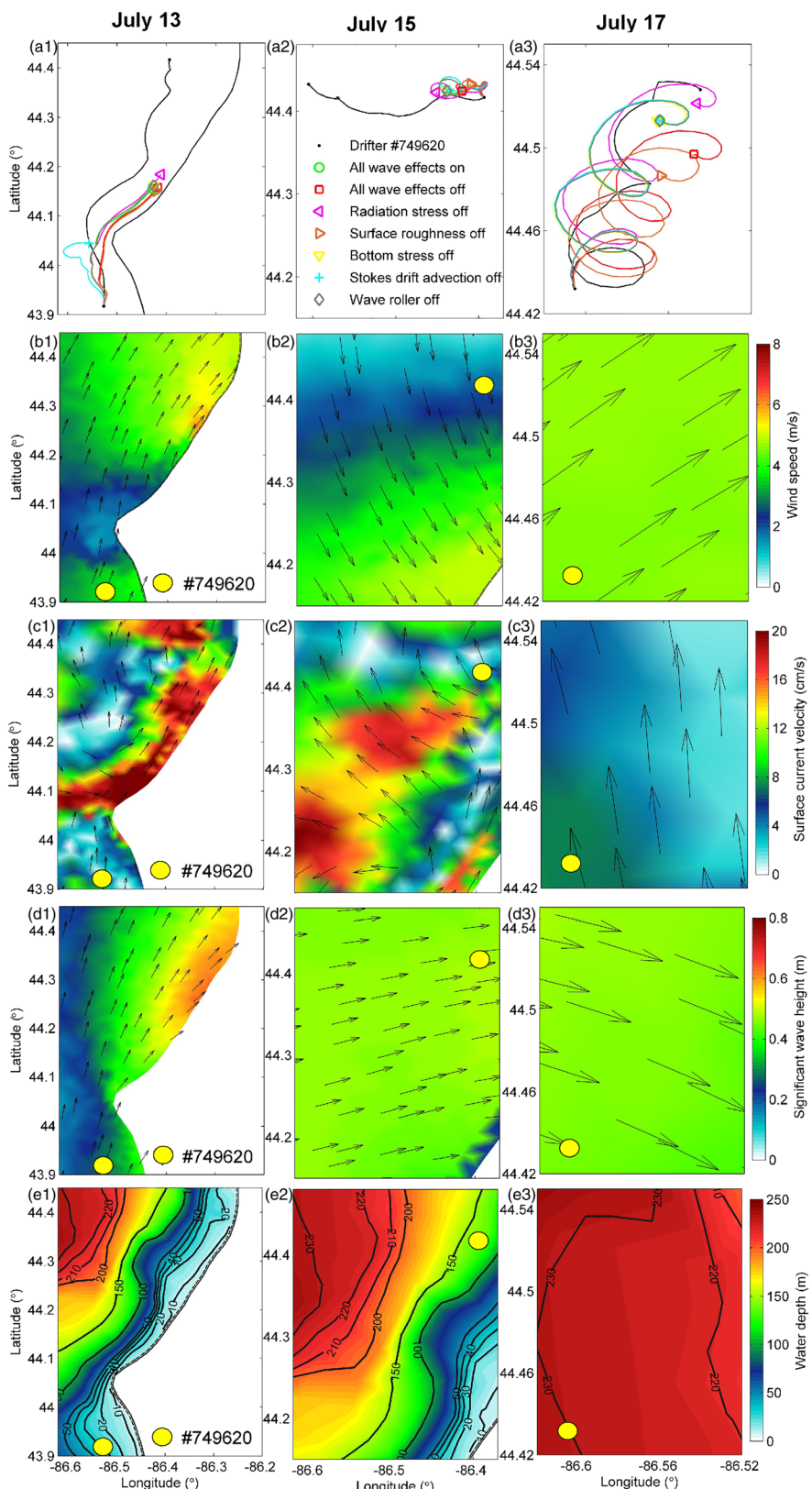


Figure 8. (a1–a3) The 2-day particle and drifter tracks, (b1–b3) wind speed, (c1–c3) surface current velocity, (d1–d3) significant wave height, and (e1–e3) water depth on (left) 13, (middle) 15, and (right) 17 July 2014, respectively.

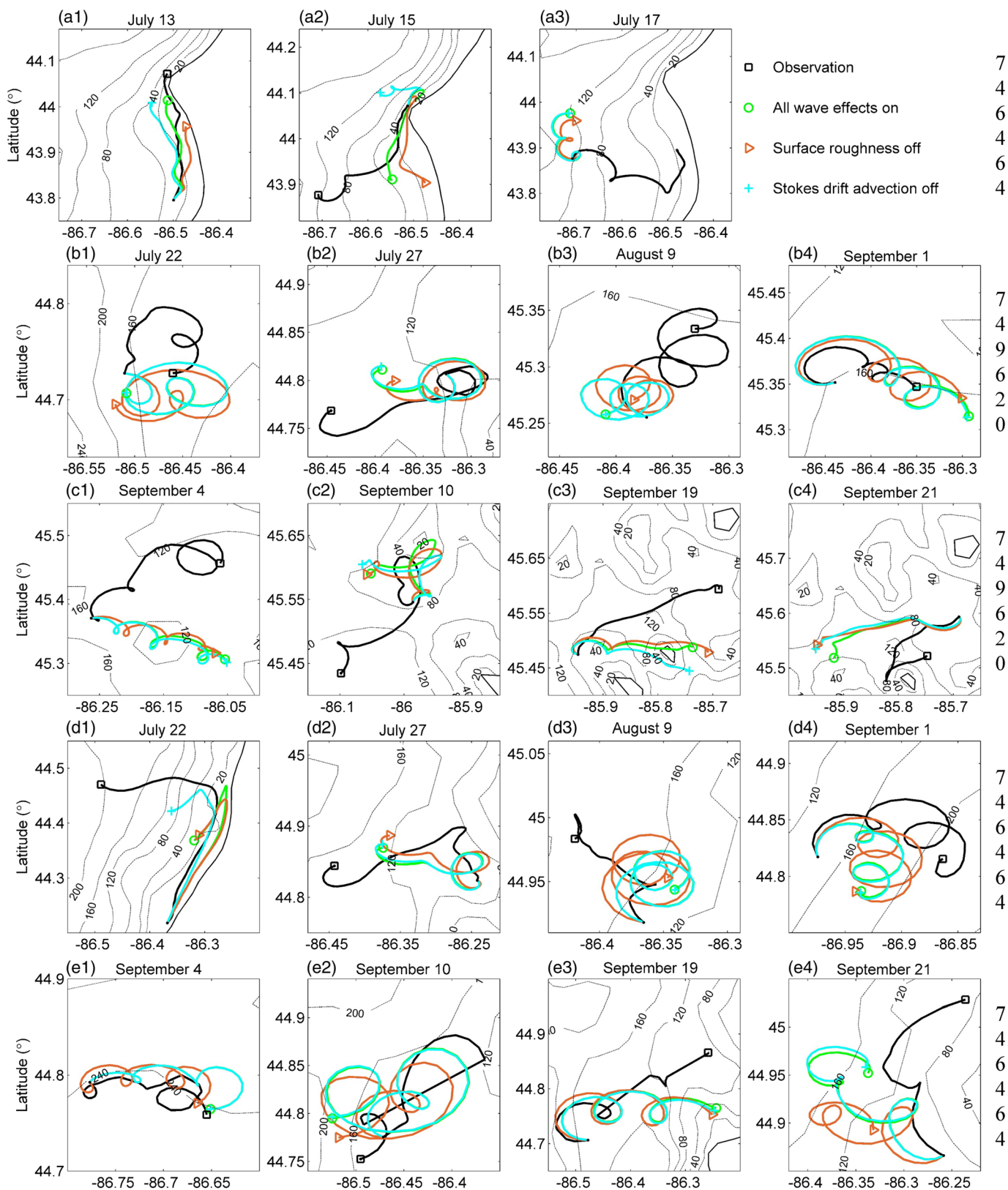


Figure 9. The 2-day particle and drifter tracks during several wind events in 2014. (a1–a3) 13–17 July for 746464; (b1–c4) 22 July to 21 September for 749620; (d1–e4) 22 July to 21 September for 746464; gray lines represent bathymetric contours.

by 4% (i.e., from 36% to 32%) during wind events (Table 3), and thus, both processes were incorporated into the modeling system. To further examine the particle sensitivity to initial sites and times (e.g., distinct trajectories and endpoints between the offshore and nearshore groups), 36 virtual particles were released near the southeastern coast in both shallow and deep-water areas from July to September 2014.

4.3. Virtual Particle Experiments

Figure 10 depicts the trajectories of 36 virtual particles released near the lake's southeastern coast. Lagrangian trajectories of the particles released at 10- to 50-m depths were mainly restricted in the shallow region with strong isobaths-following drifts and negligible offshore movements in July (Figures 10a1 and 10a2). Particles from 80-m water depth showed a slight offshore movement, and those released at 110- and 140-m depths displayed clockwise (i.e., anticyclonic) deep-lake circulation (Figure 10a2). This experiment confirms that the particle fate is largely dependent upon its distance to the adjacent coast. In August, particles released in the relatively shallow area (10–50 m) moved farther north compared to those in July (Figure 10b1), while those started at 110- and 140-m depths followed an anticlockwise (i.e., cyclonic) pattern (Figure 10b2). Particle trajectories in September (Figures 10c1 and 10c2) were more similar to those in July than August, and one uniqueness was its reversal movement during the longshore drifting period (Figure 10c1). Therefore, the particle fate starting near the lake's southeastern coast is dependent not only upon initial locations (e.g., distance near the adjacent coast) but also upon releasing times (e.g., July, August, or September) as wind and wave-induced effects are distinct on coastal dynamics.

This experiment is significant for the understanding of the connectivity between nearshore and offshore regions. The particles at 10- to 80-m depths experienced shorter traveling distances than those in deep-lake areas at 110 and 140 m (e.g., 511 vs. 726 km, see Table 4). Additionally, various movement patterns of particles led to distinct traveling distances. In July, the 10-m water depth one traveled 512 km to the north along the coast (Figure 10a1). Starting at 80-m water depth, however, its traveling distance increased to 614 km, which is attributed to additional reversal drifts and offshore movements (Figure 10a2). These phenomena suggest that the extensiveness of geographic span for the particle is highly associated with the nearshore-offshore connectivity and its initial location. The above analysis illuminated that virtual particle simulations provide an important tool toward understanding nearshore-offshore transports and spatial spreading of particles, which is particularly relevant to larval transport and settlement (Beletsky et al., 2017).

4.4. Model Uncertainties Versus Improvements From Physics Effects

Overall, the recently developed observation-modeling system has enhanced our understanding of particle dynamics. Simulations using various physics settings indicate that increased model performance relative to observations are from the improved estimation of the surface current (e.g., application of more realistic winds and air-lake fluxes, adding Stokes drift advection and wave-induced momentum terms). However, it is a difficult issue to distinguish between the actual improvements from physics effects versus uncertainties in the external forcing and model terms. Therefore, this section focuses on discussing the various uncertainties and their potential impacts on the results and conclusions.

Given that wind-driven currents play a significant role in the particle movement (Delpeche-Ellmann et al., 2016), the uncertainty of wind data sources can substantially influence the surface circulation and subsequent particle trajectory. Under strong wind conditions (e.g., the maximum wind speeds at 10-m height of 12.1 and 14.7 m/s for 2-day events on 15 and 22 July, respectively), overestimated/underestimated northerly winds along the lake's eastern coast can lead to more/less offshore particle movements. From this perspective, accurate winds likely result in a better description of nearshore dynamics. Additional particle simulations using two other favored atmospheric wind products, which include the GEM and the Climate Forecast System Version 2 (CFSv2) data, indicate that the uncertainty from wind sources leads up to 10% variations of the ensemble-averaged RSD score (Figure 11a). The deteriorated performance of particle simulations driven by the CFSv2 winds is presumably caused by the low wind quality in estimating coastal winds. The normalized Fourier norm F_n for the modeled wind speeds relative to coastal observations at MKGM4, 45024, MEEM4 from the NNM, GEM, and CFSv2 winds are 0.36, 0.63, and 0.59, respectively. The improved estimation of coastal winds from the NNM data is inherently determined by the observational data-based interpolation method, which is heavily dependent upon the limited buoys and meteorological stations at coastal land sites (Jensen et al., 2012). By contrast, the atmospherically

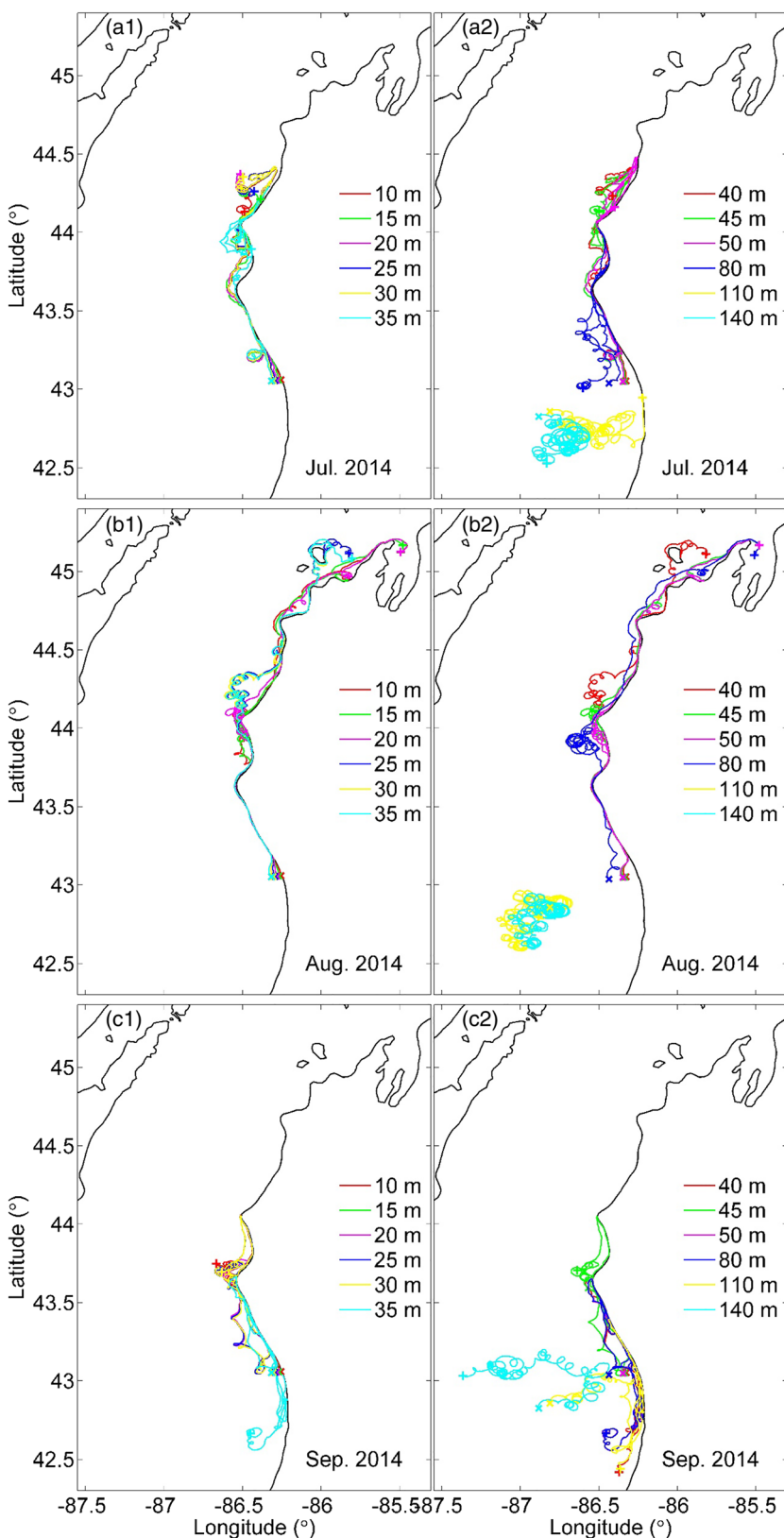


Figure 10. Simulated 1-month particle trajectories in (a1 and a2) July, (b1 and b2) August, and (c1 and c2) September 2014. Note: cross and plus signs represent the start and end points.

Table 4

Accumulated 1-Month Traveling Distances (km) of Individual Particles Released Near the Lake's Southeastern Coast at Various Locations From July to September 2014

Depth (m)	July	August	September	Mean
10	481	512	543	512
15	458	483	547	496
20	464	499	546	503
25	469	485	548	501
30	466	497	543	502
35	471	497	588	519
40	446	483	583	504
45	476	491	548	505
50	435	470	587	497
80	520	614	587	574
10–80	469	503	562	511
110	678	848	573	700
140	789	836	633	753
110–140	733	842	603	726
10–140	513	560	569	547

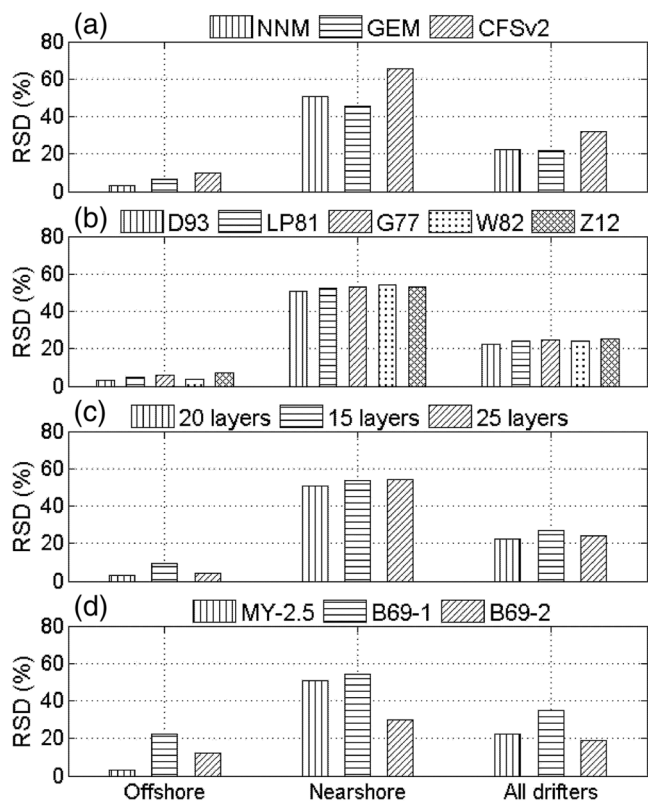


Figure 11. Ensemble-averaged RSD for the particle experiment in 2014 using (a) various wind sources, (b) wind drag coefficient formulations, (c) sigma layers, and (d) vertical mixing coefficient parameterizations.

modeled product from the GEM data have been proved to have a greater spatial coherence of the wind field and are more physically meaningful in deep-water regions, where observational buoys are less than coastal sites (Mao et al., 2016). By replacing the NNM wind with the GEM data, the RSD scores for offshore, nearshore, and all drifters are changed by 3%, -5%, and 0, respectively. Accordingly, an improved wind field can be reconstructed in the future by blending the atmospheric modeled wind products with the observational-based wind data (He et al., 2004), which is beyond the scope of this study.

In addition to the wind data used to force the model, uncertainties in estimations of wind drag coefficient can directly affect the calculated wind stress and thus modeled surface current and particle trajectories. Besides the sea state-dependent wind drag formula of Donelan et al. (1993, D93) (see Equations A9 and A10), the four most widely used methods in estimating the drag coefficient (Equations A5–A8), which include Large and Pond (1981) (LP81), Garratt (1977, G77), Wu (1982, W82), and Zijlema et al. (2012, Z12), are applied to numerical models for further discussion. Simulations show that variability of the RSD score resulting from using various wind drag coefficient formulations is as small as 3% (Figure 11b). Under strong wind conditions (e.g., 14.8 m/s on 4 July, see Figures 4d and 4e), the calculated drag coefficients from the four polynomial functions vary in a small range between 1.45×10^{-3} and 1.76×10^{-3} . However, selections of drag coefficient formulae potentially lead to substantial variations of surface flows at higher wind speed exceeding 20 m/s (Zedler et al., 2009). Regarding estimations of the wind drag coefficient based on wave-induced stress, a recently developed, physically parameterized representation of the total drag in the wave boundary layer model (including both the skin and form forces, see Donelan et al., 2012; viscous and form, see Reichl et al., 2014) was applied to investigate wave dynamics and storm surges under hurricane conditions in the open ocean (Chen & Curcic, 2016; Du et al., 2017; Shankar & Behera, 2019). Considering the high complexity of the wind drag coefficient under hurricane conditions (Powell et al., 2003), it is a worthwhile future endeavor to improve the representation of the wind drag coefficient under extremely high wind speeds with additional drifter observations.

For the vertical model grid, there are uncertainties in the vertical structure of currents in the upper several meters. The application of proper sigma layers most likely leads to a better representation of lake dynamics during the thermally stratified summer season (Niu et al., 2015). By decreasing the sigma layers from 20 to 15, the ensemble RSD increased from 22% to 27% (i.e., by 5%); this value became slightly larger when the sigma layer further increased to 25 (e.g., 24% for the RSD score, see Figure 11c). This can be explained by the fact that the calculated pressure gradient error is highly associated with sigma layer number (Mellor et al., 1994), while this error-induced inaccuracy is insignificant when the layer number exceeded 20 (Niu et al., 2015). When 15 sigma layers were applied in the vertical coordinate, the simulated Offshore Drifter 750107 showed weaker longshore movements upcoast and was stranded near the coast (not shown here) with a deteriorated RSD score of 23%

(e.g., increasing by 3%). As the sigma layer was not oriented well with the horizontal isopycnal, a possible solution to correcting the sigma layer-induced error is the adoption of z-level model, yet it may introduce additional errors near the bottom boundary level (Ezer & Mellor, 2004). Given the fact that previous studies in Lakes Michigan (Beletsky et al., 2006) and Erie (Niu et al., 2015) both have demonstrated that using the terrain-following, sigma layer-based coordinate is proper for hydrodynamic simulations and little improvement is achieved when this layer exceeds 20, the present study adopts 20 layers for particle simulations.

In the current study, the modified MY-2.5 turbulent closure model (Galperin et al., 1988) is adopted to account for the vertical mixing effect. To further study the uncertainty of near-surface flows that influence particle trajectories due to the uncertainty in the vertical mixing, alternative parameterization methods (Bryan, 1969) with constant vertical mixing coefficients K_M of 10^{-1} and $10^{-2} \text{ m}^2/\text{s}$ (B69-1 and B69-2) for coastal regions were used individually for analysis in the modeling system (Figure 11d). When the relatively larger vertical mixing coefficient $10^{-1} \text{ m}^2/\text{s}$ was used, no significant separation between the offshore and nearshore groups was detected and all drifters wandered in the southern part of the lake (not shown here). By replacing the modified MY-2.5 turbulent closure model with a constant $K_M = 10^{-1} \text{ m}^2/\text{s}$ for the vertical mixing coefficient, the ensemble-averaged *RSD* for all drifters increased from 22% to 35% (i.e., by 13%). Although the ensemble-averaged *RSD* score was reduced by 3% when a relatively weak $K_M = 10^{-2} \text{ m}^2/\text{s}$ was used, all simulated particles ended up in the offshore regions (i.e., neither being stranded around islands or ashore, not shown here). Given that the vertical mixing effect can vary significantly from nearshore to offshore regions (Rao & Schwab, 2007), especially during the stratified summer for Lake Michigan (Beletsky & Schwab, 2001), a constant vertical mixing parameter used over the entire lake is not physically reasonable. Therefore, the current study follows most previous works in the Great Lakes (Beletsky et al., 2006; Rowe et al., 2015) by adopting the modified MY-2.5 turbulence closure model for the vertical mixing scheme. In the future, a potential endeavor to obtain a more accurate vertical mixing model would be worthwhile, including the effects of surface wind-wave mixing (Bai et al., 2013) and Langmuir turbulence (D'Asaro et al., 2014; Harcourt, 2015; Li et al., 2016).

5. Summary of Findings and Study Conclusions

This study successfully applied an unstructured-grid-based wave-current coupled particle-tracking model to the nearshore of Lake Michigan, with the help of 11 surface drifter observations released near the lake's southeastern coast in the summers of 2014 and 2015. The model demonstrated its great ability in describing the drifters' movements and estimating endpoints. Additional numerical experiments were conducted to investigate the individual contributions of remote and local winds, heat flux, river inputs, and waves to particle dynamics. Virtual particles were released to examine their responses to various initial locations and releasing times. Finally, actual improvements of the modeling system from the inclusion of physics effects versus uncertainties in the model terms were discussed. The results are summarized in the following points:

1. Analysis of wind buoy data and ADCP measurements near the lake's southeastern coast suggests that coastal currents are mainly controlled by the local wind forcing and occasionally impacted by remote winds. The drifter experiment conducted in the lake's southeastern coast confirms that winds significantly impact coastal dynamics, especially for the substantial nearshore-offshore movements during strong wind events. Trajectories of surface drifters are highly sensitive to its initial locations, and endpoints of the nearshore and offshore groups are stranded in distinct regions (e.g., lake's northern part and southeastern shore, respectively).
2. Simulations demonstrate that particle fates are dominated by winds and influenced by heat flux and waves. The ensemble-averaged *RSD* from the standard run is 22%, which is increased by 33%, 5%, 14%, 5%, and 2% by excluding all, local, remote winds, heat flux, and waves, respectively. For the wave effects, both the wave-induced sea surface roughness and Stokes drift advection are key to the simulated particle trajectories (e.g., improved the *RSD* up to 21% and 38% during particular wind events and reduced the ensemble-averaged *RSD* by 4% during 11 wind events for 749620 and 746464). Additional virtual particle experiment suggests that the particle fate is dependent not only on its releasing locations (e.g., either nearshore or offshore regions) but also upon local wind conditions and wind-induced surface flows.
3. The actual model improvements are achieved by adding more physics effects and considering uncertainties. To reduce the model uncertainties, selections of high-quality wind data are critical to accurately

describing coastal currents. The observation-based NNM data show better agreements with buoy winds than the atmospheric products from CFSv2. While wind drag coefficient is important to the calculated wind stress, using different drag coefficient formations caused 3% uncertainties of the *RSD* score. By increasing the sigma layer from 15 to 20, the model resolves the surface currents better and reduces the *RSD* from 27% to 22%. For the vertical turbulent mixing parameterization, the adoption of a physically reasonable, modified MY-2.5 turbulent closure model improves the *RSD* by 13% compared to a constant vertical mixing coefficient at $10^{-1} \text{ m}^2/\text{s}$.

Dynamics of particle fates are important to understand nearshore-offshore transports, which substantially link to the larval transport, settlement, and fisheries recruitment success. The observation-modeling system can be further applied to similar freshwater bodies in the Great Lakes and estuarine environments along the U.S. East and Gulf Coast (e.g., Chesapeake Bay and Galveston Bay). The potential improvement of the observation-modeling system can be achieved by additional drifter observations in the nearshore region and by constructing a more integrated modeling system that dynamically couples atmosphere-wave-ocean interactions in the future.

Appendix A: Wave-Current Physics Terms in the Momentum Equation

A.1 Wave-Induced Stokes Drift Advection

The concept of Stokes drift advection \vec{u}_{St} derives from Stokes (1847), which is used to explain the excessive momentum transport in the propagational direction of ocean surface waves (Longuet-Higgins, 1953). Here, the vertically resolved, three-dimensional (3D), wave-induced Stokes drift advection follows the practical equation in Mellor (2015), which is represented by the hyperbolic function:

$$\vec{u}_{St} = \frac{2\vec{k}E}{c} \frac{\cosh 2|\vec{k}|D(1+\varsigma)}{\sinh 2|\vec{k}|D}, \quad (\text{A1})$$

where \vec{k} , E , and c are the wave number, wave energy, and the phase speed of waves; $|\vec{k}|$ is the magnitude of wave number \vec{k} . The wave energy is computed by $E = \frac{1}{16}gH_s^2$, in which g is the gravity constant and H_s is the significant wave height. The total water depth $D = h + \eta$ is the summation of the static mean water depth D and the time-space varying water surface elevation η . The value of sigma $\varsigma = \frac{z - \eta}{D}$ increases from -1 to 0 with a corresponding vertical coordinate z changes from $-h$ at the bottom layer to η in the surface. In the wave-current coupled model, the Lagrangian velocity with the consideration of the wave-induced Stokes drift advection $\vec{u}_L = \vec{u}_E + \vec{u}_{St}$ is used to calculate the particle trajectory. \vec{u}_E is the Eulerian current velocity, which represents the barotropic and baroclinic ocean circulation on time scales considerably longer than the period of surface gravity waves. \vec{u}_{St} is the net drift of the wave orbital velocity over the wave period under a wavy water surface (Mellor, 2015; Phillips, 1977), which is implicitly measured by the surface drifters. However, it is difficult to exactly quantify how much percentage of the wave effect is subjected. One goal of this paper is to use the numerical model, with some representations of wave-current coupled physics, to reproduce the complex drifter trajectories (e.g., experiencing an unknown combination of winds, waves, and ocean currents) as accurate as possible. It should be noted that the wind slippage effect (i.e., direct windage) on drifters has been significantly reduced by limiting their exposure to the air (Figure 2).

A.2 Wave-Induced Radiation Stress and Roller

The latest and improved formulations of the vertically resolved, three-dimensional (3D), radiation stress (Mellor, 2015) and roller (Svendsen, 1984; Svendsen et al., 2002; Warner et al., 2008) are given by:

$$\left\{ \begin{array}{l} S_{xx} = \left| \vec{k} \right| E \left[\frac{k_x^2}{\left| \vec{k} \right|^2} F_{CC} F_{CS} - F_{SS} F_{SC} + \frac{1}{2 \left| \vec{k} \right| D} \frac{\partial}{\partial \zeta} (2 F_{CC} F_{SS} - F_{SS}^2) \right] + \frac{k_x^2}{\left| \vec{k} \right|} \frac{C^2}{L} A_R R_z \\ S_{yy} = \left| \vec{k} \right| E \left[\frac{k_y^2}{\left| \vec{k} \right|^2} F_{CC} F_{CS} - F_{SS} F_{SC} + \frac{1}{2 \left| \vec{k} \right| D} \frac{\partial}{\partial \zeta} (2 F_{CC} F_{SS} - F_{SS}^2) \right] + \frac{k_y^2}{\left| \vec{k} \right|} \frac{C^2}{L} A_R R_z \\ S_{xy} = \frac{k_x k_y}{\left| \vec{k} \right|^2} F_{CC} F_{CS} + \frac{k_x k_y}{\left| \vec{k} \right|} \frac{C^2}{L} A_R R_z, \end{array} \right. \quad (A2)$$

where

$$\left\{ \begin{array}{l} F_{SS} = \frac{\sinh \left| \vec{k} \right| D (1 + \zeta)}{\sinh \left| \vec{k} \right| D} \\ F_{SC} = \frac{\sinh \left| \vec{k} \right| D (1 + \zeta)}{\cosh \left| \vec{k} \right| D} \\ F_{CS} = \frac{\cosh \left| \vec{k} \right| D (1 + \zeta)}{\sinh \left| \vec{k} \right| D} \\ F_{CC} = \frac{\cosh \left| \vec{k} \right| D (1 + \zeta)}{\cosh \left| \vec{k} \right| D}. \end{array} \right. \quad (A3)$$

The wave-induced roller is expressed together with the radiation stress (i.e., first and second term on the right side, respectively) in Equation A2. (S_{xx} , S_{yy}) represents the 3D radiation stress in the (x, y) plane, and S_{xy} is the x/y component across the y/x plane. (k_x, k_y) is the x and y components of wave number, respectively. In the 3D wave-induced roller term, the wave roller area $A_R = \frac{a}{\sqrt{2}} H_s L Q_b$ where a is a parameter with a value of 0.06 and Q_b is the fraction of breaking waves; the exponentially decaying function from the surface to bottom layer $R_z = 1 - \tanh \left(\frac{2z}{\gamma} \right)^4$, in which $\gamma = \frac{H_s}{D}$ is the ratio of significant wave height to the local water depth.

The wave-induced 3D radiation stress and roller gradients (F_x, F_y) in the momentum balance equation are expressed as:

$$\left\{ \begin{array}{l} F_x = -\frac{\partial S_{xx}}{\partial x} - \frac{\partial S_{xy}}{\partial y} \\ F_y = -\frac{\partial S_{xy}}{\partial x} - \frac{\partial S_{yy}}{\partial y}. \end{array} \right. \quad (A4)$$

A.3 Wave-Induced Sea Surface Roughness

The calculated wind drag coefficient (C_D) without the inclusion of wave-current interaction is simply a polynomial function of wind speed at 10-m height U_{10} , and the four most widely empirical formulations are developed by Garratt (1977), Large and Pond (1981), Wu (1982), and Zijlema et al. (2012). The bulk formula proposed by Garratt (1977) is the most widely used in terms of the coupled ADCIRC (Advanced Circulation Model) and SWAN system (Dietrich et al., 2010), which is given as:

$$C_D = \begin{cases} (0.75 + 0.067U_{10}) \times 10^{-3} & U_{10} < 41 \text{ m/s} \\ 3.5 \times 10^{-3} & U_{10} \geq 41 \text{ m/s} \end{cases}. \quad (\text{A5})$$

The default drag formulation in FVCOM adopts Large and Pond (1981) and can be written as:

$$C_D = \begin{cases} 1.2 \times 10^{-3} & U_{10} < 11 \text{ m/s} \\ (0.49 + 0.065 \times U_{10}) \times 10^{-3} & 11 \text{ m/s} \leq U_{10} \leq 25 \text{ m/s} \\ 2.115 \times 10^{-3} & U_{10} > 25 \text{ m/s} \end{cases}. \quad (\text{A6})$$

The major difference between Equations A5 and A6 is the upper limit of C_D , which is capped at 3.5×10^{-3} and 2.115×10^{-3} , respectively.

Another empirical relation for estimating wind drag is from Wu (1982):

$$C_D = \begin{cases} 1.2875 \times 10^{-3} & U_{10} < 7.5 \text{ m/s} \\ (0.8 + 0.065U_{10}) \times 10^{-3} & U_{10} \geq 7.5 \text{ m/s} \end{cases}, \quad (\text{A7})$$

where no upper bound is applied at high wind speed.

Zijlema et al. (2012) developed a quadratic function with a decreasing trend in the drag coefficient at high wind speed, which is expressed as:

$$C_D = \left[0.55 + 2.97 \frac{U_{10}}{U_{ref}} - 1.49 \left(\frac{U_{10}}{U_{ref}} \right)^2 \right] \times 10^{-3}. \quad (\text{A8})$$

In this expression, $U_{ref} = 31.5 \text{ m/s}$ refers to the wind speed at which C_D reaches its maximum value.

In the wave-current coupled system, the sea state-dependent wind drag coefficient is associated with the sea surface roughness z_{0s} (Donelan et al., 1993):

$$C_D = \left[\frac{\kappa}{\ln \left(\frac{10}{z_{0s}} \right)} \right]^2, \quad (\text{A9})$$

where

$$z_{0s} = \begin{cases} 3.7 \times 10^{-5} \cdot \frac{U_{10}^2}{g} \left(\frac{U_{10}}{c} \right)^{0.9} \frac{U_{10}}{c} < 10 \\ 3.7 \times 10^{-5} \cdot \frac{U_{10}^2}{g} 10^{0.9} \frac{U_{10}}{c} \geq 10. \end{cases} \quad (\text{A10})$$

κ is the von Kármán constant at 0.41, and z_{0s} is related to inverse wave age $\frac{U_{10}}{c}$. To avoid the unrealistic estimation of z_{0s} under strong wind conditions, its upper bound is set at 0.002 (Ardhuin et al., 2008).

A.4 Wave-Induced Bottom Frictional Stress

The surface wave-induced orbital motions can extend down to the bottom layer in shallow water, which is able to cause wave-bottom interactions and affect bottom frictional stress. The combined wave-averaged stress (τ_{cw}) in the current direction is parameterized by Soulsby (1997):

$$\tau_{cw} = \tau_c \left[1 + 1.2 \left(\frac{\tau_w}{\tau_c + \tau_w} \right)^{3.2} \right], \quad (\text{A11})$$

where τ_c and τ_w are the current- and wave-induced bottom frictional stresses.

Based on the wave-current boundary model of Madsen (1994), the computation of wave-induced bottom frictional stress (τ_{wx}, τ_{wy}) is as follows:

$$(\tau_{wx}, \tau_{wy}) = 0.5 \cdot f_w(u_w, v_w) \sqrt{u_w^2 + v_w^2}, \quad (\text{A12})$$

$$f_w = \begin{cases} 0.3 \frac{C_\mu u_{br}}{k_N \omega_\gamma} \leq 0.2 \\ C_\mu e^{[7.02 \left(\frac{C_\mu u_{br}}{k_N \omega_\gamma} \leq 0.2 \right)^{-0.078} - 8.82]} \quad 0.2 < \frac{C_\mu u_{br}}{k_N \omega_\gamma} < 10^2 \\ C_\mu e^{[5.61 \left(\frac{C_\mu u_{br}}{k_N \omega_\gamma} \right)^{-0.109} - 7.3]} \quad \frac{C_\mu u_{br}}{k_N \omega_\gamma} \geq 10^2, \end{cases} \quad (\text{A13})$$

$$C_\mu = (1 + 2\mu|\cos\phi_{cw}| + \mu^2)^{0.5}, \quad (\text{A14})$$

in which (u_w, v_w) and ω_γ represent the near bottom wave orbital velocity u_{br} in the (x,y) space and the radian frequency, respectively. The Nikuradse roughness k_N is 30 times the bottom roughness length z_{ob} . The piecewise function f_w is the wave friction factor depending on the relative roughness $\left(\frac{C_\mu u_{br}}{k_N \omega_\gamma}\right)$; ϕ_{cw} stands for the angle between the current and wave direction. Given that the ratio of the bottom shear stress between current and wave (μ) is much smaller than 1, the value of C_μ is set at 1.

Data Availability Statement

Simulation results produced in this work can be publicly accessed at Figshare (<https://doi.org/10.6084/m9.figshare.12366077>).

Acknowledgments

This project is funded by a National Science Foundation grant to M. Xia (1238044), and also NOAA GLERL. Dr. Xia's group helped build and deploy drifters and J. Manning of the Northeast Fishery Science Center was thanked for sharing his expertise in the design of surface drifters. D. J. Schwab is greatly appreciated for his constructive discussion with Dr. Xia on the wave-current coupled model and nearshore dynamics. Dr. S. J. Lentz hosted Dr. Xia's short visit to the Woods Hole Oceanographic Institution and provided insightful comments on drifter studies and wave-current dynamics. The authors greatly appreciated the Editor (Dr. N. Pinardi) and two anonymous reviewers for their constructive comments that significantly improved the quality of this manuscript. Numerical experiments were conducted on the CISL's Yellowstone and Cheyenne, and Stampede's HPC machines from the Texas Advanced Computing Center.

References

- Ardhuin, F., Hamon, M., Collard, F., Chapron, B., & Quefférou, P. (2008). Spectral wave evolution and spectral dissipation based on observations: A global validation of new source functions. In *Proceedings, 4th Chinese-German Joint Symposium on Coastal and Ocean Engineering*. Darmstadt, Germany.
- Bai, X., Wang, J., Schwab, D. J., Yang, Y., Luo, L., Leshkevich, G. A., & Liu, S. (2013). Modeling 1993–2008 climatology of seasonal general circulation and thermal structure in the Great Lakes using FVCOM. *Ocean Modelling*, 65, 40–63. <https://doi.org/10.1016/j.ocemod.2013.02.003>
- Beardsley, R. C., Limeburner, R., Yu, H., & Cannon, G. A. (1985). Discharge of the Changjiang (Yangtze River) into the East China Sea. *Continental Shelf Research*, 4(1-2), 57–76. [https://doi.org/10.1016/0278-4343\(85\)90022-6](https://doi.org/10.1016/0278-4343(85)90022-6)
- Beletsky, D., Beletsky, R., Rutherford, E. S., Sieracki, J. L., Bossenbroek, J. M., Chadderton, W. L., et al. (2017). Predicting spread of aquatic invasive species by lake currents. *Journal of Great Lakes Research*, 43(3), 14–32. <https://doi.org/10.1016/j.jglr.2017.02.001>
- Beletsky, D., Saylor, J. H., & Schwab, D. J. (1999). Mean circulation in the Great Lakes. *Journal of Great Lakes Research*, 25(1), 78–93. [https://doi.org/10.1016/S0380-1330\(99\)70718-5](https://doi.org/10.1016/S0380-1330(99)70718-5)
- Beletsky, D., & Schwab, D. J. (2001). Modeling circulation and thermal structure in Lake Michigan: Annual cycle and interannual variability. *Journal of Geophysical Research*, 106(C9), 19,745–19,771. <https://doi.org/10.1029/2000JC000691>
- Beletsky, D., & Schwab, D. J. (2008). Climatological circulation in Lake Michigan. *Geophysical Research Letters*, 35, L21604. <https://doi.org/10.1029/2008GL035773>
- Beletsky, D., Schwab, D. J., & McCormick, M. J. (2006). Modeling the 1998–2003 summer circulation and thermal structure in Lake Michigan. *Journal of Geophysical Research*, 111, C10010. <https://doi.org/10.1029/2005JC003222>
- Beletsky, D., Schwab, D. J., Roebber, P. J., McCormick, M. J., Miller, G. S., & Saylor, J. H. (2003). Modeling wind-driven circulation during the March 1998 sediment resuspension event in Lake Michigan. *Journal of Geophysical Research*, 108(C2), 3038. <https://doi.org/10.1029/2001JC001159>
- Bryan, K. (1969). Climate and the ocean circulation. *Monthly Weather Review*, 97(11), 806–827. [https://doi.org/10.1175/1520-0493\(1969\)097<0806:CATOC>2.3.CO;2](https://doi.org/10.1175/1520-0493(1969)097<0806:CATOC>2.3.CO;2)
- Chen, C., Beardsley, R. C., Cowles, G., Qi, J., Lai, Z., Gao, G., et al. (2013). *An unstructured grid, Finite-Volume Community Ocean Model FVCOM user manual* (3rd ed., SMAST/UMASSD Tech. Rep.-13-0701, p. 404). New Bedford, MA: University of Massachusetts Dartmouth.
- Chen, J.-L., Hsu, T.-J., Shi, F., Raubenheimer, B., & Elgar, S. (2015). Hydrodynamic and sediment transport modeling of New River Inlet (NC) under the interaction of tides and waves. *Journal of Geophysical Research: Oceans*, 120, 4028–4047. <https://doi.org/10.1002/2014JC010425>
- Chen, S. S., & Curcic, M. (2016). Ocean surface waves in Hurricane Ike (2008) and Superstorm Sandy (2012): Coupled model predictions and observations. *Ocean Modelling*, 103, 161–176. <https://doi.org/10.1016/j.ocemod.2015.08.005>
- Coelho, E. F., Hogan, P., Jacobs, G., Thoppil, P., Huntley, H. S., Haus, B. K., et al. (2015). Ocean current estimation using a multi-model ensemble Kalman filter during the Grand Lagrangian Deployment experiment (GLAD). *Ocean Modelling*, 87, 86–106. <https://doi.org/10.1016/j.ocemod.2014.11.001>

- Côté, J., Gravel, S., Méthot, A., Patoine, A., Roch, M., & Staniforth, A. (1998). The operational CMC-MRB global environmental multiscale (GEM) model. Part I: Design considerations and formulation. *Monthly Weather Review*, 126(6), 1373–1395. [https://doi.org/10.1175/1520-0493\(1998\)126<1373:TOCMGE>2.0.CO;2](https://doi.org/10.1175/1520-0493(1998)126<1373:TOCMGE>2.0.CO;2)
- Curcic, M., Chen, S. S., & Özgökmen, T. M. (2016). Hurricane-induced ocean waves and Stokes drift and their impacts on surface transport and dispersion in the Gulf of Mexico. *Geophysical Research Letters*, 43, 2773–2781. <https://doi.org/10.1002/2015GL067619>
- D'Asaro, E. A., Thomson, J., Shcherbina, A. Y., Harcourt, R. R., Cronin, M. F., Hemer, M. A., & Fox-Kemper, B. (2014). Quantifying upper ocean turbulence driven by surface waves. *Geophysical Research Letters*, 41, 102–107. <https://doi.org/10.1002/2013GL058193>
- Davis, R. E. (1985a). Drifter observations of coastal surface currents during CODE: The method and descriptive view. *Journal of Geophysical Research*, 93, 4741–4755.
- Davis, R. E. (1985b). Drifter observations of coastal surface currents during CODE: The statistical and dynamical views. *Journal of Geophysical Research*, 93, 4756–4772.
- Delpeche-Ellmann, N., Torsvik, T., & Soomere, T. (2016). A comparison of the motions of surface drifters with offshore wind properties in the Gulf of Finland, the Baltic Sea. *Estuarine, Coastal and Shelf Science*, 172, 154–164. <https://doi.org/10.1016/j.ecss.2016.02.009>
- Dietrich, J. C., Bunya, S., Westerink, J. J., Ebersole, B. A., Smith, J. M., Atkinson, J. H., & Roberts, H. J. (2010). A high-resolution coupled riverine flow, tide, wind, wind wave, and storm surge model for southern Louisiana and Mississippi. Part II: Synoptic description and analysis of hurricanes Katrina and Rita. *Monthly Weather Review*, 138(2), 378–404. <https://doi.org/10.1175/2009MWR2907.1>
- Donelan, M. A., Curcic, M., & Magnusson, A. K. (2012). Modeling waves and wind stress. *Journal of Geophysical Research*, 117, C00J23. <https://doi.org/10.1029/2011JC007787>
- Donelan, M. A., Dobson, F. W., Smith, S. D., & Anderson, R. J. (1993). On the dependence of sea surface roughness on wave development. *Journal of Physical Oceanography*, 23(9), 2143–2149. [https://doi.org/10.1175/1520-0485\(1993\)023<2143:OTDOSS>2.0.CO;2](https://doi.org/10.1175/1520-0485(1993)023<2143:OTDOSS>2.0.CO;2)
- Du, J., Bolaños, R., & Larsén, X. G. (2017). The use of a wave boundary layer model in SWAN. *Journal of Geophysical Research: Oceans*, 122, 42–62. <https://doi.org/10.1002/2016JC012104>
- Ezer, T., & Mellor, G. L. (2004). A generalized coordinate ocean model and a comparison of the bottom boundary layer dynamics in terrain-following and in z-level grids. *Ocean Modelling*, 6(3-4), 379–403. [https://doi.org/10.1016/S1463-5003\(03\)00026-X](https://doi.org/10.1016/S1463-5003(03)00026-X)
- Fringer, O. B., Dawson, C. N., He, R., & Zhang, Y. J. (2019). The future of coastal and estuarine modeling: Findings from a workshop. *Ocean Modelling*, 143, 101458. <https://doi.org/10.1016/j.ocemod.2019.101458>
- Galperin, B., Kantha, L. H., Hassid, S., & Rosati, A. (1988). A quasi-equilibrium turbulent energy model for geophysical flows. *Journal of the Atmospheric Sciences*, 45(1), 55–62. [https://doi.org/10.1175/1520-0469\(1988\)045<0055:AQETEM>2.0.CO;2](https://doi.org/10.1175/1520-0469(1988)045<0055:AQETEM>2.0.CO;2)
- Ganju, N. K., Lentz, S. J., Kirincich, A. R., & Farrar, J. T. (2011). Complex mean circulation over the inner shelf south of Martha's Vineyard revealed by observations and a high-resolution model. *Journal of Geophysical Research*, 116, C10036. <https://doi.org/10.1029/2011JC007035>
- Garratt, J. R. (1977). Review of drag coefficients over oceans and continents. *Monthly Weather Review*, 105(7), 919–929.
- Garvine, R. W. (1985). A simple model of estuarine subtidal fluctuations forced by local and remote wind stress. *Journal of Geophysical Research*, 90(C6), 11,945–11,948. <https://doi.org/10.1029/JC090iC06p11945>
- Haas, K. A., Svendsen, I. A., Haller, M. C., & Zhao, Q. (2003). Quasi-three-dimensional modeling of rip current systems. *Journal of Geophysical Research*, 108(C7), 3217. <https://doi.org/10.1029/2002JC001355>
- Hanshue, S. K., & Harrington, A. H. (2017). Grand River assessment. *Michigan Department of Natural Resources Fisheries Report* 20 (p. 537). Lansing, MI.
- Harcourt, R. R. (2015). An improved second-moment closure model of Langmuir turbulence. *Journal of Physical Oceanography*, 45(1), 84–103. <https://doi.org/10.1175/JPO-D-14-0046.1>
- He, R., Liu, Y., & Weisberg, R. H. (2004). Coastal ocean wind fields gauged against the performance of an ocean circulation model. *Geophysical Research Letters*, 31, L14303. <https://doi.org/10.1029/2003GL019261>
- Hickey, B. M., Pietrafesa, L. J., Jay, D. A., & Boicourt, W. C. (1998). The Columbia River Plume Study: Subtidal variability in the velocity and salinity fields. *Journal of Geophysical Research*, 103(C5), 10,339–10,368. <https://doi.org/10.1029/97JC03290>
- Huntley, H. S., Lippardt, B. L., & Kirwan, A. D. (2011). Lagrangian predictability assessed in the East China Sea. *Ocean Modelling*, 36(1-2), 163–178. <https://doi.org/10.1016/j.ocemod.2010.11.001>
- Jensen, R. E., Cialone, M. A., Chapman, R. S., Ebersole, B. A., Anderson, M., & Thomas, L. (2012). *Lake Michigan storm: Wave and water level modeling*. Rep. ERDC/CHL-TR-12-26, U.S. Army Eng. Res. And Dev. Cent. Coastal and Hydraul. Lab. Vicksburg, MS.
- Jordi, A., Basterretxea, G., & Wang, D.-P. (2011). Local versus remote wind effects on the coastal circulation of a microtidal bay in the Mediterranean Sea. *Journal of Marine Systems*, 88(2), 312–322. <https://doi.org/10.1016/j.jmarsys.2011.05.007>
- Large, W. G., & Pond, S. (1981). Open ocean momentum flux measurements in moderate to strong winds. *Journal of Physical Oceanography*, 11(3), 324–336. [https://doi.org/10.1175/1520-0485\(1981\)011<0324:OOMFMI>2.0.CO;2](https://doi.org/10.1175/1520-0485(1981)011<0324:OOMFMI>2.0.CO;2)
- Lee, C., Schwab, D. J., Beletsky, D., Stroud, J., & Lesht, B. (2007). Numerical modeling of mixed sediment resuspension, transport, and deposition during the March 1998 episodic events in southern Lake Michigan. *Journal of Geophysical Research*, 112, C02018. <https://doi.org/10.1029/2005JC003419>
- Lentz, S. J., & Fewings, M. R. (2012). The wind- and wave-driven inner-shelf circulation. *Annual Review of Marine Science*, 4(1), 317–343. <https://doi.org/10.1146/annurev-marine-120709-142745>
- Li, Q., Webb, A., Fox-Kemper, B., Craig, A., Danabasoglu, G., Large, W. G., & Vertenstein, M. (2016). Langmuir mixing effects on global climate: WAVEWATCH III in CESM. *Ocean Modelling*, 103, 145–160. <https://doi.org/10.1016/j.ocemod.2015.07.020>
- Liu, Y., & Weisberg, R. H. (2011). Evaluation of trajectory modeling in different dynamic regions using normalized cumulative Lagrangian separation. *Journal of Geophysical Research*, 116, C09013. <https://doi.org/10.1029/2010JC006837>
- Longuet-Higgins, M. S. (1953). Mass transport in water waves. *Philosophical Transactions. Royal Society of London*, 245, 535–581.
- Lumpkin, R., Özgökmen, T., & Centurioni, L. (2017). Advances in the application of surface drifters. *Annual Review of Marine Science*, 9(1), 59–81. <https://doi.org/10.1146/annurev-marine-010816-060641>
- Madsen, O. S. (1994). Spectral wave-current bottom boundary layer flows. In *Coastal Engineering 1994, Proceedings of the 24th International Conference, Coastal Engineering Research Council* (pp. 384–398). Kobe, Japan: American Society of Civil Engineers.
- Mao, M., van der Westhuysen, A. J., Xia, M., Schwab, D. J., & Chawla, A. (2016). Modeling wind waves from deep to shallow waters in Lake Michigan using unstructured SWAN. *Journal of Geophysical Research: Oceans*, 121, 3836–3865. <https://doi.org/10.1002/2015JC011340>
- Mao, M., & Xia, M. (2017). Dynamics of wave-current-surge interactions in Lake Michigan: A model comparison. *Ocean Modelling*, 110, 1–20. <https://doi.org/10.1016/j.ocemod.2016.12.007>
- Mao, M., & Xia, M. (2018). Wave-current dynamics and interactions near the two inlets of a shallow lagoon-inlet-coastal ocean system under hurricane condition. *Ocean Modelling*, 129, 124–144. <https://doi.org/10.1016/j.ocemod.2018.08.002>

- Mayer, D. A., Weisberg, R. H., Zheng, L., & Liu, Y. (2017). Winds on the West Florida Shelf: Regional comparisons between observations and model estimates. *Journal of Geophysical Research: Oceans*, 122, 834–846. <https://doi.org/10.1002/2016JC012112>
- McCormick, M. J., Manley, T. O., Beletsky, D., Foley, A. J. III, & Fahnstiel, G. L. (2008). Tracking the surface flow in Lake Champlain. *Journal of Great Lakes Research*, 34(4), 721–730. [https://doi.org/10.1016/S0380-1330\(08\)71613-7](https://doi.org/10.1016/S0380-1330(08)71613-7)
- McCormick, M. J., Miller, G. S., Murthy, C. R., Rao, Y. R., & Saylor, J. H. (2002). Tracking coastal flow with surface drifters during the episodic events: Great Lakes experiment. *Verhandlungen des Internationalen Verein Limnologie*, 28, 365–369.
- Mellor, G. L. (2015). A combined derivation of the integrated and vertically resolved, coupled wave-current equations. *Journal of Physical Oceanography*, 45(6), 1453–1463. <https://doi.org/10.1175/JPO-D-14-0112.1>
- Mellor, G. L., Ezer, T., & Oey, L.-Y. (1994). The pressure gradient conundrum of sigma coordinate ocean models. *Journal of Atmospheric and Oceanic Technology*, 11(4), 1126–1134. [https://doi.org/10.1175/1520-0426\(1994\)011<1126:TPGCOS>2.0.CO;2](https://doi.org/10.1175/1520-0426(1994)011<1126:TPGCOS>2.0.CO;2)
- Nekouee, N., Hamidi, S. A., Roberts, P. J. W., & Schwab, D. J. (2015). A coupled empirical-numerical model for a buoyant river plume in Lake Michigan. *Water, Air, and Soil Pollution*, 226(12), 412. <https://doi.org/10.1007/s11270-015-2676-z>
- Nekouee, N., Roberts, P. J. W., Schwab, D. J., & McCormick, M. J. (2013). Classification of buoyant river plumes from large aspect of ratio channels. *Journal of Hydraulic Engineering*, 139(3), 296–309. [https://doi.org/10.1061/\(ASCE\)HY.1943-7900.0000651](https://doi.org/10.1061/(ASCE)HY.1943-7900.0000651)
- Nguyen, T. D., Thupaki, R., Anderson, E. J., & Phanikumar, M. S. (2014). Summer circulation and exchange in the Saginaw Bay-Lake Huron system. *Journal of Geophysical Research: Oceans*, 119, 2713–2734. <https://doi.org/10.1002/2014JC009828>
- Niu, Q., & Xia, M. (2017). The role of wave-current interaction in Lake Erie's seasonal and episodic dynamics. *Journal of Geophysical Research: Oceans*, 122, 7291–7311. <https://doi.org/10.1002/2017JC012934>
- Niu, Q., Xia, M., Ludsin, S. A., Chu, P. Y., Mason, D. M., & Rutherford, E. S. (2018). High-turbidity events in Western Lake Erie during ice-free cycle: Contributions of river-loaded vs. resuspended sediment. *Limnology & Oceanography*, 63(6), 2545–2562.
- Niu, Q., Xia, M., Rutherford, E. S., Mason, D. M., Anderson, E. J., & Schwab, D. J. (2015). Investigation of interbasin exchange and interannual variability in Lake Erie using an unstructured-grid hydrodynamic model. *Journal of Geophysical Research: Oceans*, 120, 2212–2232. <https://doi.org/10.1002/2014JC010457>
- Phillips, O. M. (1977). The dynamics of surface waves. *The dynamics of the upper ocean* (2nd ed., pp. 33–98). Cambridge, UK: Cambridge University Press.
- Powell, M. D., Vickery, P. J., & Reinhold, T. A. (2003). Reduced drag coefficient for high wind speeds in tropical cyclones. *Nature*, 422(6929), 279–283. <https://doi.org/10.1038/nature01481>
- Prakash, S., Atkinson, J. F., & Green, M. L. (2007). A semi-Lagrangian study of circulation and transport in Lake Ontario. *Journal of Great Lakes Research*, 33(4), 774–790. [https://doi.org/10.3394/0380-1330\(2007\)33\[774:ASSOCA\]2.0.CO;2](https://doi.org/10.3394/0380-1330(2007)33[774:ASSOCA]2.0.CO;2)
- Rao, Y. R., & Schwab, D. J. (2007). Transport and mixing between the coastal and offshore waters in the Great Lakes: A review. *Journal of Great Lakes Research*, 33(1), 202–218. [https://doi.org/10.3394/0380-1330\(2007\)33\[202:TAMBTC\]2.0.CO;2](https://doi.org/10.3394/0380-1330(2007)33[202:TAMBTC]2.0.CO;2)
- Reichl, B. G., Hara, T., & Ginis, I. (2014). Sea state dependence of the wind stress over the ocean under hurricane winds. *Journal of Geophysical Research: Oceans*, 119, 30–51. <https://doi.org/10.1002/2013JC009289>
- Röhrs, J., Christensen, K. H., Hole, L. R., Broström, G., Drivdal, M., & Sundby, S. (2012). Observation-based evaluation of surface wave effects on currents and trajectory forecasts. *Ocean Dynamics*, 62(10–12), 1519–1533. <https://doi.org/10.1007/s10236-012-0576-y>
- Rowe, M. D., Anderson, E. J., Wang, J., & Vanderploeg, H. A. (2015). Modeling the effect of invasive quagga mussels on the spring phytoplankton bloom in Lake Michigan. *Journal of Great Lakes Research*, 41, 49–65. <https://doi.org/10.1016/j.jglr.2014.12.018>
- Rypina, I. I., Kirincich, A., Lentz, S., & Sundermeyer, M. (2016). Investigating the eddy diffusivity concept in the coastal ocean. *Journal of Physical Oceanography*, 46(7), 2201–2218. <https://doi.org/10.1175/JPO-D-16-0020.1>
- Saha, S., Moorthi, S., Xu, X., Wang, J., Nadiga, S., Tripp, P., et al. (2014). The NCEP Climate Forecast System Version 2. *Journal of Climate*, 27(6), 2185–2208. <https://doi.org/10.1175/JCLI-D-12-00823.1>
- Schwab, D. J. (1983). Numerical simulation of low-frequency current fluctuations in Lake Michigan. *Journal of Physical Oceanography*, 13(12), 2213–2224. [https://doi.org/10.1175/1520-0485\(1983\)013<2213:NSOLFC>2.0.CO;2](https://doi.org/10.1175/1520-0485(1983)013<2213:NSOLFC>2.0.CO;2)
- Schwab, D. J., & Morton, J. A. (1984). Estimation of overlake wind speed from overland wind speed: A comparison of three methods. *Journal of Great Lakes Research*, 10(1), 68–72. [https://doi.org/10.1016/S0380-1330\(84\)71808-9](https://doi.org/10.1016/S0380-1330(84)71808-9)
- Shankar, C. G., & Behera, M. R. (2019). Wave boundary layer model based wind drag estimation for tropical storm surge modelling in the Bay of Bengal. *Ocean Engineering*, 191, 106509. <https://doi.org/10.1016/j.oceaneng.2019.106509>
- Smagorinsky, J. (1963). General circulation experiments with the primitive equations: I. The basic experiment. *Monthly Weather Review*, 91(3), 99–164. [https://doi.org/10.1175/1520-0493\(1963\)091<099:GCEWTP>2.3.CO;2](https://doi.org/10.1175/1520-0493(1963)091<099:GCEWTP>2.3.CO;2)
- Soulsby, R. (1997). Combined waves and currents. In *Dynamics of Marine Sands. A manual for practical applications* (pp. 87–95). London, UK: Thomas Telford Publishing.
- Stewart, R. H. (2008). *Introduction to physical oceanography*. College Station, TX: Dep. of Oceanogr., Tex. A&M Univ.
- Stokes, G. G. (1847). On the theory of oscillatory waves, *Trans. Cambridge Philos., Soc.*, 8, 441.
- Svendsen, I. A. (1984). Wave heights and set-up in a surfzone. *Coastal Engineering*, 8(4), 303–329. [https://doi.org/10.1016/0378-3839\(84\)90028-0](https://doi.org/10.1016/0378-3839(84)90028-0)
- Svendsen, I. A., Haas, K., & Zhao, Q. (2002). Theoretical background. *Quasi-3D nearshore circulation model SHORECIRC, user's manual, Version 2.0* (pp. 5–21). Newark: Center for Applied Coastal Research, Department of Civil Engineering, University of Delaware.
- SWAN Group (2012a). SWAN Scientific and Technical Documentation—SWAN Cycle III Version 40.91, chap. 3, pp. 43–51, Delft Univ. of Technol., Delft, Netherlands. [Available at <http://www.swan.tudelft.nl/>.]
- SWAN Group (2012b). SWAN User Manual—SWAN Cycle III Version 40.91, chap. 4, pp. 55–56, Delft Univ. of Technol., Delft, Netherlands. [Available at <http://www.swan.tudelft.nl/>.]
- Tang, C. L., Perrie, W., Jenkins, A. D., DeTracey, B. M., Hu, Y., Toulany, B., & Smith, P. C. (2007). Observation and modeling of surface currents on the Grand Banks: A study of the wave effects on surface currents. *Journal of Geophysical Research*, 112, C10025. <https://doi.org/10.1029/2006JC004028>
- Troy, C. D., Ahmed, S., Hawley, N., & Goodwell, A. (2012). Cross-shelf thermal variability in southern Lake Michigan during the stratified periods. *Journal of Geophysical Research*, 117, C02028. <https://doi.org/10.1029/2011JC007148>
- Van Sebille, E., Griffies, S. M., Abernathey, R., Adams, T. P., Berloff, P., Biastoch, A., et al. (2018). Lagrangian ocean analysis: Fundamentals and practices. *Ocean Modelling*, 121, 49–75. <https://doi.org/10.1016/j.ocemod.2017.11.008>
- Warner, J. C., Sherwood, C. R., Signell, R. P., Harris, C. K., & Arango, H. G. (2008). Development of a three-dimensional, regional, coupled wave, current, and sediment transport model. *Computational Geosciences*, 34(10), 1284–1306. <https://doi.org/10.1016/j.cageo.2008.02.012>

- Weisberg, R. H., & He, R. (2003). Local and deep-ocean forcing contributions to anomalous water properties on the West Florida Shelf. *Journal of Geophysical Research*, 108(C6), 3184. <https://doi.org/10.1029/2002JC001407>
- Whitney, M. M., & Garvine, R. W. (2006). Simulating the Delaware Bay buoyant outflow: Comparison with observations. *Journal of Physical Oceanography*, 36(1), 3–21. <https://doi.org/10.1175/JPO2805.1>
- Wu, J. (1982). Wind-stress coefficients over sea surface from breeze to hurricane. *Journal of Geophysical Research*, 87(C12), 9704–9706. <https://doi.org/10.1029/JC087iC12p09704>
- Xia, M., Xie, L., & Pietrafesa, L. J. (2007). Modeling of the Cape Fear River Estuary plume. *Estuaries and Coasts*, 30(4), 698–709. <https://doi.org/10.1007/BF02841966>
- Xia, M., Xie, L., & Pietrafesa, L. J. (2010). Winds and the orientation of a coastal plane estuary plume. *Geophysical Research Letters*, 37, L19601. <https://doi.org/10.1029/2010GL044494>
- Xia, M., Xie, L., Pietrafesa, L. J., & Whitney, M. M. (2011). The ideal response of a Gulf of Mexico estuary plume to wind forcing: Its connection with salt flux and a Lagrangian view. *Journal of Geophysical Research*, 116, C08035. <https://doi.org/10.1029/2010JC006689>
- Yu, J., & Slinn, D. N. (2003). Effects of wave-current interaction on rip currents. *Journal of Geophysical Research*, 108(C3), 3088. <https://doi.org/10.1029/2001JC001105>
- Zedler, S. E., Niiler, P. P., Stammer, D., Terrill, E., & Morzel, J. (2009). Ocean's response to Hurricane Frances and its implications for drag coefficient parameterization at high wind speeds. *Journal of Geophysical Research*, 114, C04016. <https://doi.org/10.1029/2008JC005205>
- Zijlema, M. (2010). Computation of wind-wave spectra in coastal waters with SWAN on unstructured grids. *Coastal Engineering*, 57(3), 267–277. <https://doi.org/10.1016/j.coastaleng.2009.10.011>
- Zijlema, M., van Vledder, G. P., & Holthuijsen, L. H. (2012). Bottom friction and wind drag for wave models. *Coastal Engineering*, 65, 19–26. <https://doi.org/10.1016/j.coastaleng.2012.03.002>